



Deep Learning Based Reduced Order Model for Airfoil-Gust and Aeroelastic Interaction

R. Halder,* M. Damodaran,† and B. C. Khoo‡

National University of Singapore, Singapore 117575, Republic of Singapore

<https://doi.org/10.2514/1.J059027>

This work aims to model transonic airfoil-gust interaction and the gust response on transonic aileron-buzz problems using high-fidelity computational fluid dynamics (CFD) and the Long Short Term Memory (LSTM) based deep-learning approach. It first explores the rich physics associated with these interactions, which show strong flowfield nonlinearities arising from the complex shock-boundary-layer interactions using CFD. In the transonic regime, most linear reduced-order models (ROMs) fail to reconstruct the unsteady global parameters such as the lift, moment, and drag coefficients and the unsteady distributive flow variables such as velocity, pressure, and skin friction coefficients on the airfoil or in the entire computational domain due to the nonlinear shock-gust interaction. As it is well known that a deep-learning framework creates several hypersurfaces to generate a nonlinear functional relationship between the gust or structural input and the unsteady flow variables, an algorithm is proposed to overcome the limitations of linear ROMs. This algorithm consists of two integral steps, namely, a dimensionality reduction where the Discrete Empirical Interpolation Method based linear data compression approach is applied and the reduced state is trained using the LSTM based Recurrent Neural Network for the reconstruction of unsteady flow variables. The present work shows its potential for predicting transonic airfoil gust response and the aileron-buzz problem demonstrating several orders of computational benefit as compared to high-fidelity CFD.

Nomenclature

AOA_{gust}	=	equivalent angle of attack for gust input
ΔC_f	=	difference between steady and unsteady coefficient of skin friction
$C_{M,\alpha}$	=	moment coefficient
ΔC_p	=	difference between steady and unsteady coefficient of pressure
f	=	gust profile
I_a	=	moment of inertia about hinge axis
M_∞	=	freestream Mach number
Re	=	freestream Reynolds number
t_{begin}	=	gust load start time
v_{g0}	=	gust amplitude
x_{begin}	=	gust start location
β	=	aileron motion
λ	=	gust length
φ	=	Discrete Empirical Interpolation Method modes

I. Introduction

GUST load analysis of aerodynamic configurations arising from atmospheric disturbances is an important design consideration in the aerospace industry. The Federal Aviation Regulations [1] stipulates that the aircraft must be subjected to different discrete and continuous gust loads of different amplitude, shape, and length at the early design stage, which is a very sophisticated and iterative process. The linear potential aerodynamic models such as the doublet lattice methods are routinely used for several applications outlined by Albano and Rodden [2]. However, low-fidelity models are reliable only in the flight Mach regimes which follow linear dynamical

relationships with input excitation, i.e., fully subsonic or supersonic flow till Mach 5. Hence, computational fluid dynamics (CFD) analysis for gust load is required in the nonlinear transonic regime where shock waves, expansion waves, and shock-wave-boundary-layer interaction render the flow nonlinear. In the potential aerodynamic analysis, the gust velocity is introduced in the flowfield by modifying the far-field boundary conditions, while for high-fidelity CFD models, a numerical approach for accounting the gust velocity in the computational domain is not so trivial. Sitaraman and Baeder [3] introduced a field velocity method (FVM) for gust load computation considering the gust velocity as the negative of the mesh velocity in the arbitrary Lagrangian–Eulerian (ALE) formulation of the Navier–Stokes equations. Another approach is the split velocity method outlined by Wales et al. [4] where the velocity variables are divided into two terms, one containing the gust velocity and, another, the velocity variable subtracted by the gust velocity terms, thereby introducing source terms in the Navier–Stokes solver to account for the presence of the gust in the flowfield. Although these CFD methods are quite effective in accounting for compressibility and viscous effects, they are computationally very expensive when it comes to the design optimization of aircraft wings.

High-speed aileron-buzz phenomena on the other hand typically can result in violent control surface deflection compromising its structural integrity and resulting in a possibly catastrophic loss of the entire aircraft. The classification of this phenomenon on the basis of types of shock motion is outlined by Lambourne [5]. Erickson and Stephenson [6] concluded based on the wind-tunnel experiments on a semispan P-80 aircraft wing that the control surface buzz is one degree of freedom flutter excluding the degree of freedom associated with wing flexibility. Typically, the upward or downward movement of a control surface is accompanied by the rearward or forward movement of the shock wave sitting on the upper and lower surfaces of the wing surface. Aileron motion causes disturbance in the pressure field, inducing further shock motion, resulting in a self-induced vibration of the control surface which often causes aeroelastic instability with a sudden increment of the amplitude of the deflecting control surface which leads to buzz. The computational study of the transonic aileron buzz problem by Steger and Bailey [7] predicted the flutter boundary considering only the aileron motion and it was observed that at a certain Mach number, oscillations in the inviscid simulation decay, while viscous simulation provides a stable limit cycle oscillation. At higher Mach numbers, the inviscid flow computation will cause a divergence of wing oscillation, but the viscous effect will lead to a stable oscillation. Hence, the effect of viscosity has a significant effect

Received 9 September 2019; revision received 24 April 2020; accepted for publication 24 April 2020; published online 11 August 2020. Copyright © 2020 by the American Institute of Aeronautics and Astronautics, Inc. All rights reserved. All requests for copying and permission to reprint should be submitted to CCC at www.copyright.com; employ the eISSN 1533-385X to initiate your request. See also AIAA Rights and Permissions www.aiaa.org/randp.

*Graduate Student, Department of Mechanical Engineering, Faculty of Engineering, 9 Engineering Drive 1; e0010762@nus.edu.

†Senior Research Scientist, Temasek Laboratories, Faculty of Engineering, 9 Engineering Drive 1; tslmura@nus.edu.sg. Associate Fellow AIAA.

‡Professor of Mechanical Engineering and Director Temasek Laboratories, Faculty of Engineering, 9 Engineering Drive 1. tshead@nus.edu.sg.

on the limit cycle position. Bendiksen [8] investigated nonclassical control surface buzz without considering the viscous effect at higher Mach number, and Bendiksen [9] studied the effect of shock motion on transonic flutter due to wing flexibility. Rampurawala [10] reports nonclassical buzz analysis considering wing flexibility in a supersonic wing showing a decrease in buzz boundary due to wing flexibility effect. As high-fidelity simulations of these problems are computationally intensive, an economic alternative will be to consider the reduced-order models and also machine-learning approaches which are being considered within the scientific machine-learning framework.

The reduced-order model (ROM), which provides a quick and reasonably accurate prediction and reconstruction of unsteady flowfield over a wide range of parametric variations, such as those pioneered by Raveh [11,12] are effective for gust response modeling. The linearized ROMs based on convolution as outlined by Ghoreyshi et al. [13] and autoregressive moving average by Raveh [11] are dynamically linear but statically nonlinear, which means that the steady-state features derive from a nonlinear model while governed by a linear time dynamics. Williams et al. [14] considered the Eigen-System Realisation Algorithm-based linearized nonintrusive approach for gust modeling past a rigid and elastically mounted airfoil. Timme et al. [15] linearized the governing equations and applied the proper orthogonal decomposition (POD) based intrusive approach for the generation of linear ROM for gust modeling. Although these linearized ROMs are generated from signals computed from a Navier–Stokes solver, these ROMs are linear about the steady state. Hence, in several situations such as the high angle of attack or large amplitude gust input, this approach does not give satisfactory estimates due to the flow separation and induced nonlinearity in the flowfield. These ROMs were developed for the computation of integrated force coefficients like lift and moment coefficients under small unsteady gust or structural inputs. If the distributive forces such as pressure field over the airfoil surface or the flow variables of the complete flow domain are to be reconstructed, the linearized ROM is not suitable because of the inherent nonlinearity of the local variables as opposed to the integrated forces which show linear relationships with the change in dynamics. Very recently, Bekemeyer et al. [16] proposed a nonlinear ROM based on a greedy search approach that is intrusive in nature.

In recent years, deep learning (DL) has proven to be very effective in several applications ranging from general regression and classification problems to image recognition and from acoustic modeling to cancer detection as outlined by Schmidhuber [17]. The conventional computational-fluid-dynamics-based approach applies to the well-posed problem with proper initial and boundary conditions. On the other hand, learning-based algorithms like deep learning are very convenient for ill-posed problems such as inverse problems, regression problems, etc., which have gained significant attention in several fluid mechanics applications. Very recently, Brunton et al. [18] described several categories of machine learning such as supervised, semisupervised, and unsupervised, based on the extent of data available for the learning process and their corresponding applications in fluid mechanics. Parish and Duraisamy [19] have proposed a field inversion and machine-learning approach, which uses data from the sources like high-fidelity simulation or experiments to generate the improved closure models for turbulence and various computational physics applications. Maulik et al. [20] have also demonstrated a neural-network-based turbulence closure model through grid-resolved information using the snapshots from the high-fidelity numerical data. Studies involving new approaches for learning feature dynamics using dimensionality reduction algorithm and deep neural network for applications in fluid dynamics include the combined POD-LSTM network of Wang et al. [21] for incompressible flow applications and the spectral proper orthogonal decomposition (SPOD) coupled with deep learning by Lui and Wolf [22]. The Physics Informed Neural Network introduced by Raissi [23] is motivating developments in scientific machine learning which maintains a tradeoff between the availability of the data and the accuracy of the solution. In the present work, the LSTM network is coupled with the Discrete Empirical Interpolation Method (DEIM) algorithm outlined as a nonlinear model order reduction framework by

Chaturantabut and Sorensen [24] to predict the nonlinear interaction of a gust with a rigid airfoil and aerostructural interaction.

There appears to be a paucity in the literature of highly nonlinear gust interaction above a certain Mach number. The main contribution of the present work is to introduce deep-learning-based nonlinear ROM, namely, the DEIM LSTM, to analyze the transonic airfoil gust response with structural interaction and also the aileron-buzz response. Application of deep learning in gust load analysis is introduced in the present work, perhaps for the first time as per the authors' knowledge. The current work is organized as follows. Section II outlines the computational framework for modeling transonic airfoil-gust and aileron-buzz response. Section III introduces DL networks and shows how this is incorporated with a ROM. Section IV discusses and demonstrates the effectiveness of this DEIM-LSTM model in predicting reliable results.

II. Numerical Methods

This work investigates the gust load effect on a rigid airfoil and a one degree of freedom aeroelastic system leading to aileron buzz in transonic flow. The open-source CFD solver SU2 described by Economou et al. [25] solves the unsteady compressible Navier–Stokes equations formulated on an ALE reference frame. It uses the Spalart–Allmaras [26] turbulence model for closure to obtain both the high-fidelity solutions and the training signals computation for the ROM framework. A FVM as outlined by Sitaraman and Baeder [3] which accounts for both the gust load effect and the structural interaction in the ALE framework is adopted in the current work. In this method, gust velocity $v_{g,j}$ is considered as the negative of grid velocity in the ALE formulation of Navier–Stokes equations. This formulation is necessary to guarantee a divergence-free gust velocity field, i.e., $\nabla \bullet \mathbf{v}_{g,j} = 0$. It also eliminates the requirement of small grid size in the entire computational domain to avoid artificial dissipation swamping the nonzero divergence term. For stationary airfoil, the grid velocity is the negative of gust velocity, i.e., $\dot{u}_\Omega = -v_g$. If only the airfoil moves without any gust load as in the case of a self-induced motion or buzz response, the mesh velocity $\dot{u}_\Omega = v_{\text{airfoil}}$. For the case of a combined structural motion and gust load interaction $\dot{u}_\Omega = -v_g + v_{\text{airfoil}}$. The ALE formulation of the flow equations expressed in a finite volume formulation takes the form

$$\iiint_{\Omega(t)} \frac{\partial W}{\partial t} d\Omega + \oint_{(F_{\text{ALE}}^c(W) - F^v(W))} \hat{n} \bullet dS = 0 \quad \text{in } \Omega \times [0, t] \quad (1)$$

where W is the vector of flow variables F_{ALE}^c and F^v is the convective and the diffusive terms defined as follows:

$$W = \begin{bmatrix} \rho \\ \rho \mathbf{v} \\ \rho E \end{bmatrix}, \quad F_{\text{ALE}}^c = \begin{bmatrix} \rho(\mathbf{v} - \mathbf{v}_{\text{airfoil}} + \mathbf{v}_{g,j}) \\ \rho \mathbf{v} \otimes (\mathbf{v} - \mathbf{v}_{\text{airfoil}} + \mathbf{v}_{g,j}) + \bar{I} p \\ \rho(\mathbf{v} - \mathbf{v}_{\text{airfoil}} + \mathbf{v}_{g,j})E + p \mathbf{v} \end{bmatrix},$$

$$F^v = \begin{bmatrix} 0 \\ \bar{\tau} \\ \bar{\tau} \bullet \mathbf{v} + \mu_{\text{tot}}^* C_{\text{pres}} \nabla T \end{bmatrix} \quad \text{and} \quad \mu_{\text{tot}}^* = \frac{\mu_{\text{dyn}}}{Pr_{\text{dyn}}} + \frac{\mu_{\text{turb}}}{Pr_{\text{turb}}}$$

Here, ρ is the fluid density, \mathbf{v} is velocity vector, p is pressure field, T is the temperature field, E is the specific total energy, and τ is the viscous stress tensor. The total dynamic viscosity μ_{tot} consists of laminar and turbulent viscosity coefficients, and C_{pres} is the specific heat of air at constant pressure. Pr_{dyn} and Pr_{turb} stand for the laminar and turbulent Prandtl number, respectively. The boundary conditions imparted to the Navier–Stokes solver are the no-slip boundary condition and adiabatic wall condition at the airfoil and characteristics-based farfield condition at the freestream boundary. The convective terms in Eq. (1) show the most general case; i.e., the airfoil is subjected to both the gust load and the structural interaction. The gust velocity is a spatiotemporal variable defined as

$$v_{g,j}(x, t) = v_{g,0} f(2\pi(x - x_{\text{begin}} - U_\infty(t - t_{\text{begin}}))/\lambda) \quad (2)$$

The gust velocity amplitude is defined in terms of the equivalent angle of attack AOA_{gust} as follows:

$$\tan(\text{AOA}_{\text{gust}}) = \frac{v_{g0}}{U_\infty} \quad (3)$$

All flow variables appearing in Eqs. (1–3) are scaled using the characteristics variables defined by Economou et al. [25]. Figure 1 shows the schematic of the gust interaction with aileron-buzz problem. A partition-based algorithm, as discussed by Piperno et al. [27], is used to handle the two-way coupling at the fluid–structure interface for the high-fidelity model. For the training signal of ROM, the governing ALE solver is prescribed with a specified structural motion. A spring-analogy-based solver as outlined by Degand and Farhat [28] is used for the mesh movement with the geometric conservation law enforced to confirm that the surface swept by the nodes of each cell equals the deformed cell volume. For such a spring-analogy-based solver, v_{airfoil} stands for the mesh velocity due to the airfoil movement, whereas in the case of rigid mesh motion, it equals the airfoil velocity. The convective part is discretized using the JST (Jameson-Schmidt-Turkel) scheme used in Economou et al. [25], maintaining a second-order spatial accuracy. Second-order dual time marching scheme is considered for the time marching of the flow solver.

In the current work, a NACA0012 airfoil is used with aileron at the 3/4th location of the chord length. The aileron buzz is modeled like the one degree of freedom motion about the hinge as follows:

$$\begin{aligned} I_\beta \ddot{\beta} &= M_\beta \\ M_\beta &= \frac{1}{2} \rho_\infty U_\infty^2 L A_{\text{ref}} C m_{\text{hinge}} \end{aligned} \quad (4)$$

I_β is the structural moment of inertia, and β is the angle of rotation of the aileron about the hinge axis. M_β and $C m_{\text{hinge}}$ are the hinge moment and moment coefficient (clockwise positive), respectively; ρ_∞ is freestream density. The values of airfoil length L and reference area A_{ref} are 1 m and 1 m^2 , respectively. The squared radius of gyration ($r_\beta^2 = I_\beta / m_a b^2$) or nondimensional structural moment of inertia is taken as 0.01292, where mass per unit span m_a is 24.28 kg/m , and the half-chord-length b is 0.5 m. Equation (4) is discretized using second-order backward Euler time marching scheme as proposed by Alonso and Jameson [29] rendering the numerical scheme to be second order in both space and time.

III. Reduced-Order Modeling

This section proposes a nonlinear ROM for the reconstruction of aerodynamic variables for the continuous gust load and the aerostructural interaction. The model reduction approach is generally catered into two broad categories, namely, the intrusive approach and non-intrusive approach. In the case of the intrusive ROM, the governing equations are projected on a few sets of reduced basis or modes φ resulting in significant changes in the source codes. The intrusive approach for nonlinear model reduction is extensively explored in the literature such as the Gauss–Newton Approximated Tensor (GNAT) scheme of Carlberg et al. [30] and the DEIM algorithm of Chaturantabut and Sorensen [24].

A finite difference discretization of the scalar nonlinear variable results in a system of nonlinear ODEs of the form with proper initial conditions:

$$\dot{x}(t) = f(x(t)) \quad (5)$$

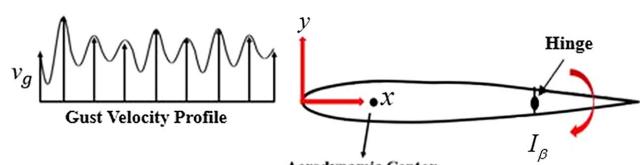


Fig. 1 Schematic of the gust interaction with aileron buzz.

Here, $t \in [0, T]$ denotes time, and $x(t) = [x_1(t), \dots, x_n(t)] \in \mathbb{R}^n$ and f is a nonlinear function acting on the $x(t)$ componentwise. The variable $x(t)$ consists of a steady-state part and an unsteady counterpart $x = \bar{x} + \hat{x}$. The state variable x is projected on an orthonormal reduced basis φ which follows the property $\varphi \varphi^T = I$ and $x = \bar{x} + \varphi h$ where h is the reduced state of the variable x and $h \in \mathbb{R}^m$, where $m \ll n$,

$$\begin{aligned} \frac{dx}{dt} &= f(\bar{x} + \varphi h) \text{ or } \varphi \frac{dh}{dt} = f(\bar{x} + \varphi h) \\ \frac{dh}{dt} &= \varphi^T f(\bar{x} + \varphi h) \end{aligned} \quad (6)$$

The computation of the nonlinear function f is still expensive as demonstrated by Chaturantabut and Sorensen [24], and it is further approximated using the DEIM or GNAT algorithm and feed to the governing Eq. (6) at each time step of the CFD based temporal marching as

$$\frac{dh}{dt} = \psi^T \hat{f}(x) \quad (7)$$

where \hat{f} is the reduced form of the high-dimensional nonlinear function f and ψ is the modified basis vector after the conversion of the computationally expensive f to the comparatively less expensive \hat{f} . The details of the DEIM algorithm will be discussed subsequently.

The nonintrusive approach, on the other hand, is data driven, and a surrogate model is generated from the high-fidelity CFD-based training input and output signals, thereby resulting in minimal changes in the flow solver. The presence of flow discontinuities like shock motion in the transonic regime causes numerical stability issues for the projection-based intrusive approaches, whereas nonintrusive approaches are quite robust in this flow regime. For a nonintrusive reduced-order approach, the variable x is first reduced to h using the DEIM or GNAT algorithm, and then the dynamic features are reconstructed by a learning algorithm. In the current work, both the global aerodynamic coefficients such as lift coefficient Cl , moment coefficient Cm , and distributive variables such as the unsteady counterparts of the C_p and C_f distributions as demonstrated in Eq. (5), i.e., ΔC_p and ΔC_f distributions, respectively [i.e., the unsteady part is analogous to \hat{x} in Eq. (5)], are reconstructed using the proposed ROM. The major building blocks of the proposed algorithm such as the training dataset generation, DEIM algorithm for dimensionality reduction, and the deep-learning approach for learning feature dynamics are elaborated in the following sections.

A. Training Dataset Generation

The most important step of the nonintrusive reduced-order model (NIROM) is the generation of the training datasets for aerodynamics. First, a steady-state transonic flowfield around the airfoil corresponding to a Mach number and angle of attack is computed. Next, the airfoil is excited with arbitrary structural inputs and gust loading corresponding to a range of different arbitrary v_{g0} and λ . The corresponding ΔC_p and ΔC_f distributions from these unsteady responses generate the corresponding dataset $D(t, \mu)$ for the future training and construction of the NIROM. If the total number of global time steps in the training signal is n_t , then the size of the dataset will be $D \in \mathbb{R}^{n \times n_t}$, where n is the total number of computational grid locations. For the case of reconstructing the global coefficients, the size of the dataset will be $D \in \mathbb{R}^{n_t}$, and since it is already integrated spatially, it does not require any further dimensionality reduction which will be discussed later in the section and directly to be fed to the deep-learning network.

B. Dimensionality Reduction

The manifold hypothesis outlined by Bengio et al. [31] forms the basis of dimensionality reduction which states that the solution of a high-dimensional dynamical system lies near a low-dimensional manifold S embedded in a large dataset of size R^n . The DEIM is a data compression method which can reconstruct the full dataset from

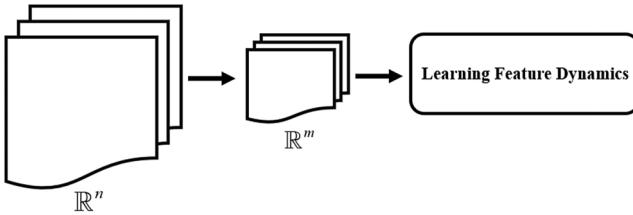


Fig. 2 The basic outline of the nonintrusive ROM combining dimensionality reduction and learning algorithm

the information of the flow variables specified at a few sensor locations. For example, if the dataset D is a function of time t or any parameter μ , then D can be expressed as $D(t) \approx \varphi c(t)$ where φ defines the DEIM modes and $c(t)$ is the coefficient vector which is computed from an index matrix or mask matrix P used for indexing sensor locations in the computational domain. The index matrix is defined as $P = [e_{\rho_1}, \dots, e_{\rho_l}]$, $P \in \mathbb{R}^{n \times l}$, where each column is defined as $e_{\rho_i} = [0, \dots, 0, 1, \dots, 0]^T$, which implies a value of 1 at location ρ_i , which is decided from an error-minimization-based algorithm as shown by Chaturantabut and Sorensen [24]. Hence, the full dataset can be approximated as

$$D(t, \mu) \approx U(P^T U)^{-1} P^T D(t, \mu) \quad (8)$$

Here, U consists of the basis vectors computed from the dataset D , $U(P^T U)^{-1}$ is considered as the DEIM modes φ , and $P^T D(t)$ indicates the sensor locations values which form the coefficient vector c . For the large datasets, the CUR approximate matrix decomposition using the DEIM algorithm as outlined by Sorensen and Embree [32] can also be used to compute the control points efficiently. The basic construct of the NIROM, resulting in dimensional reduction from R^n to R^m , is shown in Fig. 2. The size of an actual dataset is n , and the size of the reduced dataset is m , where $m \ll n$. This reduced dataset is fed to a deep-learning algorithm for exploring the feature dynamics of the system as outlined in Sec. III.C. A series of snapshots, each having the size of R^n is reduced to a set of snapshots of the size of R^m before feeding in the deep-learning network.

C. Learning Feature Dynamics

The learning of the unsteady training data using a deep-learning network, which is a computational graph consisting of several nodes among which the information gets propagated is accomplished as follows. The basic structure of a neural network consists of three fundamental layers, i.e., the input layer x , the hidden layer h , and the output layer y . The input will be the structural deflection or the gust velocity input $\in \mathbb{R}^{n_t}$. There are several possibilities for the output layer. One possibility can be $y \in \mathbb{R}^{N \times n_t}$ consisting of the distributive variables ΔC_p and ΔC_f distribution on the airfoil surface at N_{dist} DEIM control points on the surface of the airfoil chosen for the estimation of distributive variables and the local Mach numbers in the entire flow domain or $y \in \mathbb{R}^{n_t}$ consisting of the global coefficients, i.e., hinge moment coefficient for aileron-buzz response and the C_l and C_m response for the airfoil-gust interaction. The total number of global time steps considered in the high-fidelity computation of the training signal is defined as n_t . The reconstruction of global coefficients is therefore classified into two groups, i.e., the reconstruction of global coefficients for rigid airfoil gust response, followed by the structural deflection input, and finally

for the combined structural deflection input and gust profile load. F_{gust} and $F_{structure}$ are the functional relationship between input gust and structural interaction x_{gust} and $x_{structure}$, respectively, and corresponding aerodynamic forces and moments obtained from the trained neural network, as shown in Figs. 3a and 3b.

To generate these functional relationships effectively using the deep-learning platform, the first simplest feedforward network as outlined by San and Maulik [33] and its extension to the Recurrent Neural Network (RNN) outlined by Wang et al. [18] and Cho et al. [34] are briefly reviewed in the context of the proposed algorithm. A nonlinear affine transformation of the input through a single-layer nonlinear function \hat{y} is defined as

$$C_l \text{ or } C_m = f(Wx + b) \quad (9)$$

where f is a nonlinear activation function as outlined by Shwartz and Ben-David [35], W is the weight matrix $\in \mathbb{R}^{M \times n_t}$, and b is bias vector $\in \mathbb{R}^M$. If there are multiple layers, the input of layer l is fed to the next layer $l + 1$. Now, the input of hidden layer h is generated from the output of the previous layers,

$$h_{l+1} = f_{l+1}(W_l f_l(\dots(f_1(W_0 x + b_0)) + \dots + b_{l-1}) + b_l) \quad (10)$$

In a general network, the training algorithm involves an optimization problem to optimize the set of parameters $\Theta = [b_i, W_i]_{i=1}^L$ by minimizing a loss function $L(f(x; \theta), y)$, which is a distance metric between the truth y and predicted data f . The optimized θ , i.e., θ^* , is defined as

$$\theta^* = \arg \min[L(f(x; \theta), y)] \quad (11)$$

The ADAM optimization algorithm, which is a stochastic gradient descent approach, as outlined by Kingma and Ba [36], is used for the minimization of the loss function. This added advantage in RNN over the feedforward network, on the other hand, is achieved by extra feedback coming from the previous time steps or previous outputs inside the network structure, as shown in Fig. 4.

The nonlinear transformation of the input sequence through the hidden layers is defined as

$$h^{n+1} = f(Wh^n + Ux^n + b) \quad (12)$$

Here, x is the input to the recurrent network, h is the hidden layer, b is the bias vector, and W and U are the weight matrices associated with the hidden layer and input vector, respectively. The RNN generally handles the sequential inputs and outputs for the training, and therefore the network can be unwrapped in a time sequence as shown in Fig. 5, and each output of the hidden layer (h_0, h_1, \dots, h_t) is multiplied with the U matrix and sent as feedback to the next layer, thereby resulting in the most suitable deep-learning algorithm for the time series type datasets. The loss function is designed for the RNN network to optimize the parameter space $\theta = [b_i, U_i, W_i]_{i=1}^k$, similar to the feedforward network in Eq. (11) with an added set of matrix entry U , which takes care of the feedback loop in the RNN architecture. In the ADAM optimization framework, the gradient of the loss function, which is generated using backpropagation as outlined by Werbos [37] can be written as $(\partial L / \partial W) = \sum_{j=0}^{n_t-1} (\partial L_j / \partial W)$ for the RNN network. It creates instances of vanishing or exploding

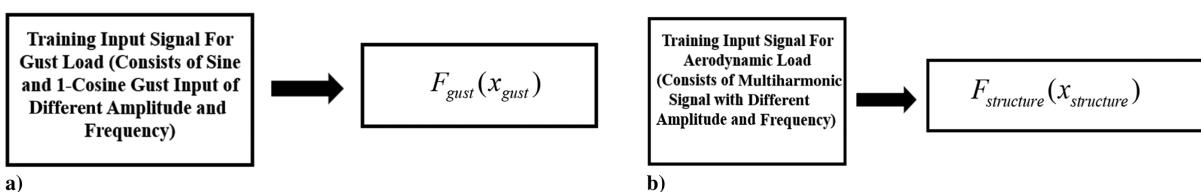


Fig. 3 Functional relationship between the aerodynamic variables and the a) gust load input on a rigid wing and b) structural input excitation.

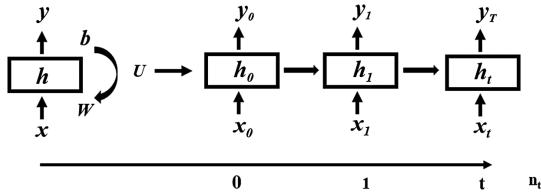


Fig. 4 Feedback from previous time steps in RNN structure.

gradient problems as demonstrated by Lipton et al. [38] because of the long-term dependencies over time-sequential dataset (multiplication of gradient terms over total time step n_t in a sequence prediction). Therefore, the LSTM network demonstrated by Hochreiter and Schmidhuber [39] is introduced in the RNN architecture to reduce this problem of vanishing or exploding gradients. Unlike the conventional RNN which keeps its contents of previous time steps while computing the gradients, the LSTM introduces four distinct operations in each RNN cell: memory cell, input gate, forget gate, and output gates. The detail of the memory cell, input gate, forget gate, and output gate and hidden layer in connection with the LSTM network is defined as follows:

$$\begin{aligned} \text{Input Gate: } i^n &= \sigma(W_i h^{n-1} + b_i) \\ \text{Forget Gate: } f^n &= \sigma(W_f h^{n-1} + b_f) \\ \text{Output Gate: } o^n &= \sigma(W_o h^{n-1} + b_o) \\ \text{Cell State: } c^n &= i^n \odot c^{n-1} + f^n \odot \tanh(W_c h^{n-1} + b_c) \\ \text{Hidden Layer: } h^n &= o^n \odot \tanh(c^n) \end{aligned} \quad (13)$$

Here, \odot is the Hadamard product; the structural input β and the gust velocity v_g are fed to the LSTM network at each step of the input sequence defined as n ; i is the input gate, and f is the forget gate, which will choose the necessary information to be passed through or forget through cell state c ; W_i , W_f , and W_c are the corresponding weight matrices; b_i , b_f , and b_o are the bias vectors for the input, forget, and cell gates, respectively. The output gate o , on the other hand, decides the control of the flow of the information from the cell state to the next hidden layer. These operations thereby help the LSTM cells to keep only the necessary memories, thereby mitigating the chances of the exploding and vanishing gradient problem in the backpropagation algorithm for each iteration step of the gradient descent optimization. Figure 5 shows the RNN architecture for the

reconstruction of the unsteady global coefficients. Figures 6 and 7 show the flowchart for the reconstruction of the unsteady global coefficients using the LSTM network and the distributive variables using the DEIM-LSTM network.

The LSTM and DEIM-LSTM networks will be used for the nonlinear ROM used in the current study for the discussion for the computation of the global and distributed loads respectively. The first and major step toward the formation of a successful neural network concerns the input and output sequence generation. The input β or v_g as shown in Figs. 5 and 6b must be provided in a batch or a fixed step size, which must be maintained to achieve an effectively trained network. The input β or the v_g vector needs to be organized in a matrix format, the demonstration of which is carried out in terms of β as input and Cl as output as follows:

Input in vector format	Input in matrix format	Output
$\begin{bmatrix} \beta_1 \\ \beta_2 \\ \beta_3 \\ \vdots \\ \beta_{n_t} \end{bmatrix}$	$\begin{bmatrix} \beta_1 & \beta_2 & \beta_3 & \dots & \beta_{\text{step}} \\ \beta_2 & \beta_3 & \beta_4 & \dots & \beta_{\text{step}+1} \\ \beta_3 & \beta_4 & \beta_5 & \dots & \beta_{\text{step}+2} \\ \vdots & \vdots & \vdots & \ddots & \vdots \\ \beta_{n_t} & \beta_{n_t+1} & \beta_{n_t+2} & \dots & \beta_{n_t+\text{step}-1} \end{bmatrix}$	$\begin{bmatrix} Cl_{\text{step}} \\ Cl_{\text{step}+1} \\ Cl_{\text{step}+2} \\ \vdots \\ Cl_{n_t+\text{step}-1} \end{bmatrix}$

(15)

The reconstruction of the distributive variables is demonstrated in Fig. 6a, which shows the overall coupling of the dimensionality reduction approach with the LSTM network, and Fig. 6b shows the details of the network architecture. Once the ΔC_p and ΔC_f distributions over the airfoil or the Mach contour in the flow domain are obtained at the control points from the network, the DEIM control point values are multiplied with DEIM modes φ as shown in Fig. 6a to reconstruct the full distributive variable. The input sequence $\{x_1, \dots, x_{n_t}\}$ corresponds to a signal length of n_t , given to the CFD solver for the generation of the output response. $\{N_{\text{dist},i=1}, \dots, N_{\text{dist},i=m}\}$ are the output sequence for the distributive variables, where m is the number of DEIM modes φ chosen and each $N_{\text{dist},i=1, \dots, m}$ will be a vector of size R^{n_t} .

IV. Results and Discussions

In this section, predictions of transonic airfoil gust response and aileron-buzz response using the high-fidelity CFD-based result and deep-learning-based reduced-order modeling outlined in the previous sections are presented and discussed. The high-fidelity CFD-based result is first used to explore the physics involved with aileron gust

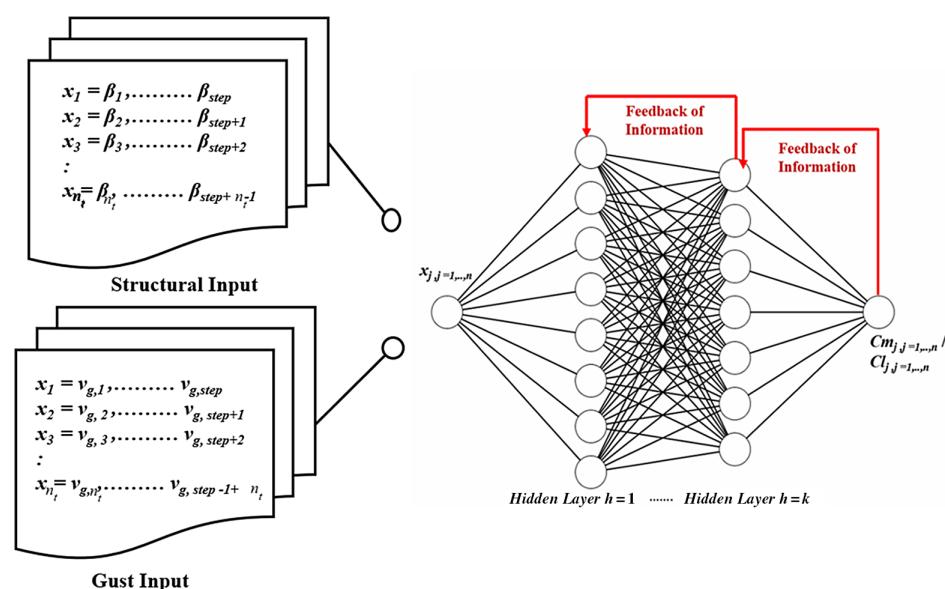


Fig. 5 RNN architecture (LSTM used in the current work is a variation of the RNN network) for the reconstruction of unsteady global variables.

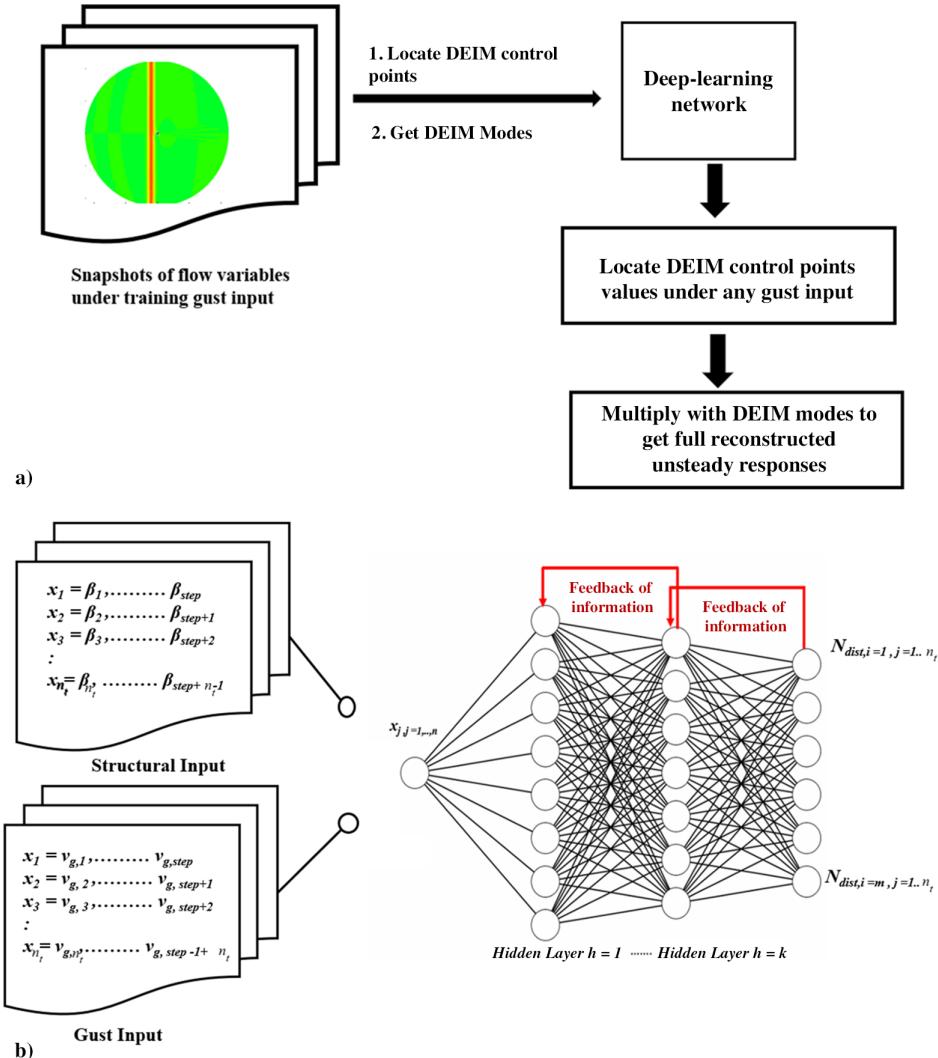


Fig. 6 a) Overall flowchart of the DEIM-LSTM nonlinear ROM and b) RNN architecture (LSTM used in the current work is a variation of RNN network) for the reconstruction of unsteady distributive variables.

and aileron buzz and to generate training data for the deep-learning networks. This is followed by a discussion on the effectiveness of linear ROM for different Mach regimes. The proposed nonlinear ROM is then applied for the cases corresponding to a Mach number near 0.85, where strong nonlinearity arises due to the shock-gust-boundary-layer interaction leading to the failure of the linear ROM in reconstructing this nonlinear interaction. In each section, the gust load on the rigid airfoil and aerostructural interaction will be outlined. For the present CFD-based numerical computation, the global time step in dual time marching algorithm is considered as 0.001745.

A. CFD-Based High-Fidelity Computation

In this section, the high-fidelity CFD-based solution of gust response on the rigid airfoil and aileron-buzz response is computed. The first test case involves the gust input, whereas the second one involves only the structural input to the aerodynamic system. The computational domain, mesh, and validation of CFD solver in generating the transonic flow-field data are discussed in section SM1 in the Supplemental Material accompanying This work. If the airfoil immersed in a freestream transonic flow at an M_∞ of 0.854 and Re of 10^7 is excited with the training signal corresponding to the gust velocity as shown in Fig. 7a, then the corresponding global coefficient output of the lift and moment coefficient are shown in Figs. 7b and 7c, respectively. The C_l response as shown in Fig. 7b is one order larger than the C_m coefficient demonstrated in Fig. 7c since the moment coefficient is computed at the aerodynamic center located at the quarter-chord position from the

leading edge of the airfoil. The gust front starts at the leading edge or x_{begin} of 0.0 at t_{begin} following the convention of Raveh [11].

The corresponding contours of the v velocity (i.e., y component of the total velocity) due to arbitrary training gust signal and corresponding shock-boundary-layer interaction are shown in Fig. 8a at the instant when the leading edge of the airfoil first encounters the gust. The v -velocity contours shown in Fig. 8a undergo modification in the vicinity of the airfoil as a result of the vertical gust velocity, which is incorporated in the ALE formulation of the Navier-Stokes equations. The contour level is reduced to 5 to -5 to highlight the gust front in the v -velocity field since the gust load component is very small as compared to the total v velocity near the airfoil. The butterfly-shaped v -velocity field over the airfoil is due to the curvature of the airfoil. Figure 8b shows the corresponding local Mach number contours in the vicinity of the trailing edge of the airfoil showing the flow circulation at the foot of the shock due to adverse pressure gradient at this particular M_∞ . This flow circulation induces nonlinearity in the flow physics, and the interaction of gust velocity input with the corresponding global force coefficients and distributive variables cannot be explored with a linear dynamical relationship.

Next, high-fidelity training datasets are developed for exciting the aerodynamics along with the structural input for modeling the flow physics of the transonic aileron-buzz response. Figure 9a shows the training structural input signal corresponding to the buzz of the trailing edge angle β , and the corresponding output variation of the hinge moment coefficient $C_{m,hinge}$ is shown in Fig. 9b at M_∞ of 0.854 and a Re of 10^7 .

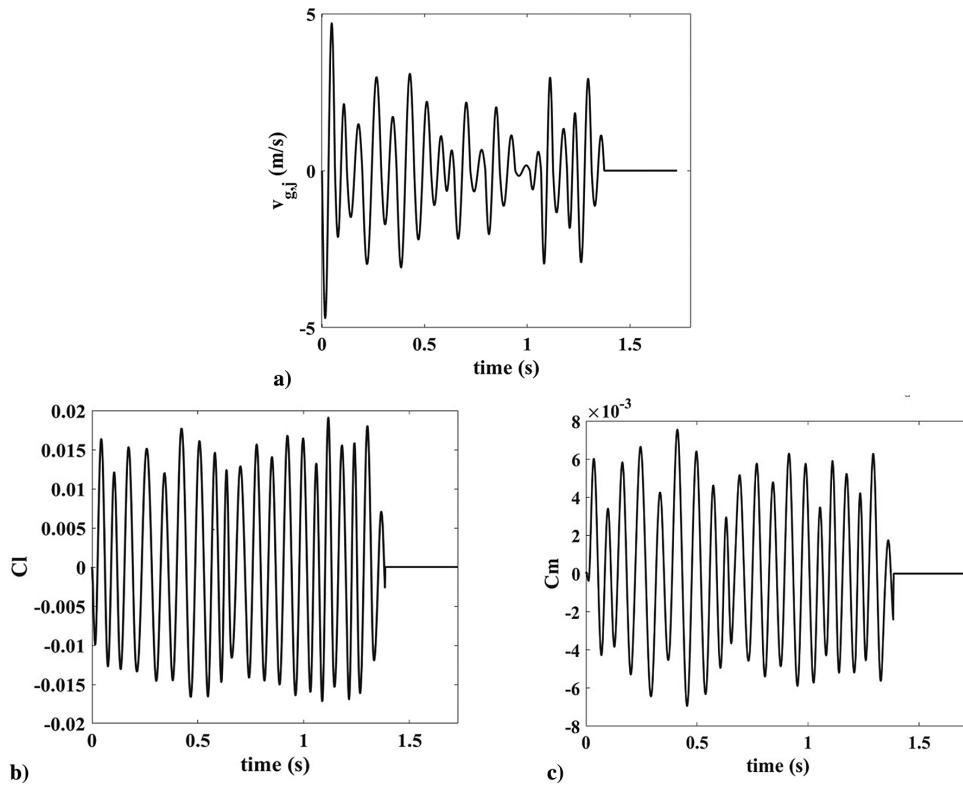


Fig. 7 (a) The input training gust velocity input to the aeroelastic system and the corresponding response of (b) global Cl coefficient and (c) global Cm coefficient of the aeroelastic system in transonic flow at M_∞ of 0.854 and Re of 10^7 .

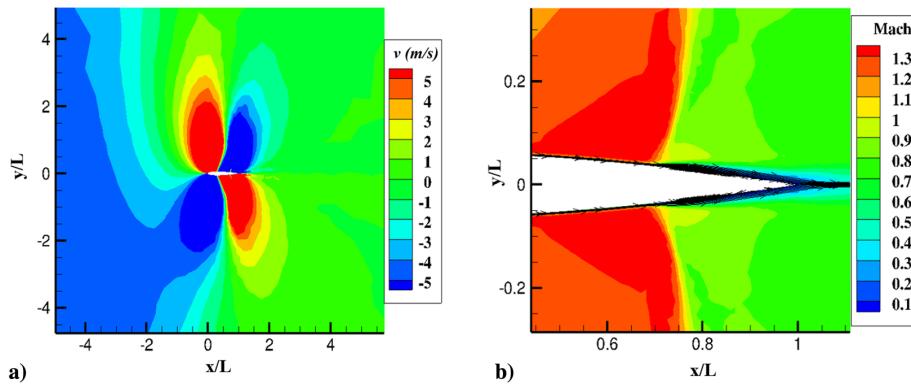


Fig. 8 Flow field contours of a) v velocity field and b) Mach with the stream traces at the foot of the shock at the instant when the training gust input signal first encounters the leading edge of the airfoil at a freestream M_∞ of 0.854 and Re of 10^7 .

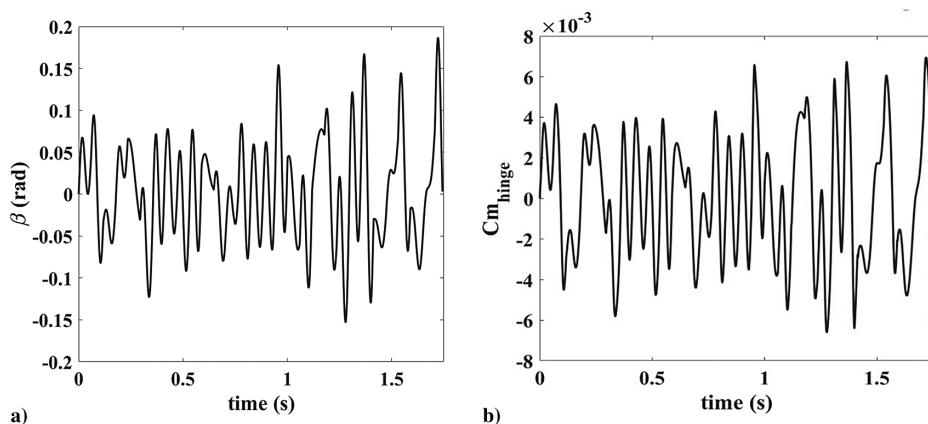


Fig. 9 a) The structural input to the aerodynamic system and b) the corresponding global hinge moment coefficient Cm_{hinge} variation is shown for the airfoil at a freestream M_∞ of 0.854 and Re of 10^7 .

The transonic aileron-buzz response is generally a self-induced postflutter instability which is caused by the free interaction between the ambient aerodynamic flowfield and the motion of the aileron relative to the main airfoil. The position of shock in the vicinity of the hinge decides the stability envelope associated with aileron buzz. The shock location gets modified due to the viscous interaction. The shock location corresponding to the case of the airfoil at a freestream M_∞ of 0.854 is shown in Fig. S5 in the Supplemental Material. The shock location corresponding to the inviscid transonic flow precedes the shock position corresponding to the viscous transonic flow at this Mach number, indicating that for inviscid transonic flow, the aileron movement becomes unstable, whereas for viscous transonic flow, it is necessary for the airfoil to be inclined at a fixed angle of attack of about 2 deg in order to achieve a limit cycle oscillation (LCO) response. Figures 10a and 10b show the diverging and decaying responses of the aileron buzz at M_∞ of 0.854 and 0.853, respectively. Different types of mesh size are used for both cases to understand the effect of the shock location on the aeroelastic response. At M_∞ of 0.854, the shock location differs with the mesh size and thereby results in different diverging responses. It is evident from Fig. 10a that the slightest variation of the shock location results in completely different diverging responses and as the amplitude of the aileron increases the structural responses deviate from each other. On the other hand, at M_∞ of 0.853, the structural responses are decaying, and the amplitudes are very small, resulting in minimal variations of the amplitude with the change in mesh size variations. This observation concludes that the flutter envelope for the inviscid flowfield condition lies in between M_∞ of 0.853 and 0.854 and at zero preset angle of attack. For viscous transonic flow at an M_∞ of 0.86 and angle of attack of 2 deg, the LCO response is shown in Fig. 11. Since a preset angle of 2 deg is maintained to generate the buzz response for viscous transonic flow cases, the structural response will not be symmetric about y axis of value zero.

For the aileron-buzz case, the freestream velocity is fixed at sea level conditions, i.e., density of 1.225 kg/m^3 and temperature of 288.25 K unlike the two degree of freedom airfoil pitch plunge system addressed by Karnick and Venkatraman [40], where freestream velocity is modified to reach the flutter envelope at a particular M_∞ . The fixed angle of attack is changed to attain a LCO response in the current situation. The viscous and inviscid CFD solver with dynamic meshing which has been validated in the previous work of the current authors, i.e., Halder et al. [41], is used for generating the high-fidelity solutions for all the current problems of interest. Figure S6 in the Supplemental Material shows the computed Mach contours with stream traces at different positions of the aileron-buzz cycle. For all subsequent studies of this problem, only the viscous transonic flow will be considered.

B. Limitations of Linear ROM Predictions

The subspace-identification-based linear ROM outlined by Halder et al. [41] has been instrumental in the regime where the

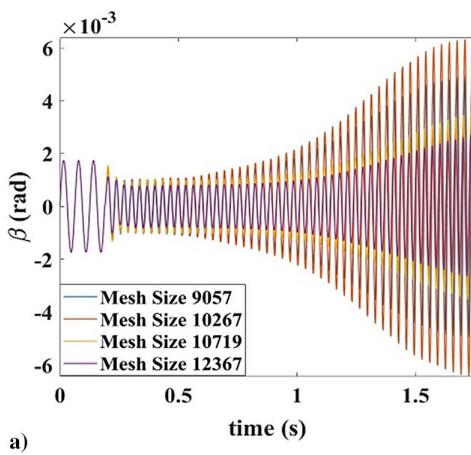


Fig. 10 a) Diverging aeroelastic response at M_∞ of 0.854 and b) decaying aeroelastic response at M_∞ of 0.853 considering inviscid flowfield assumption.

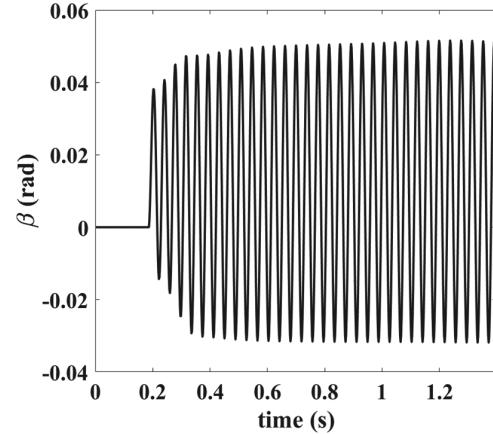
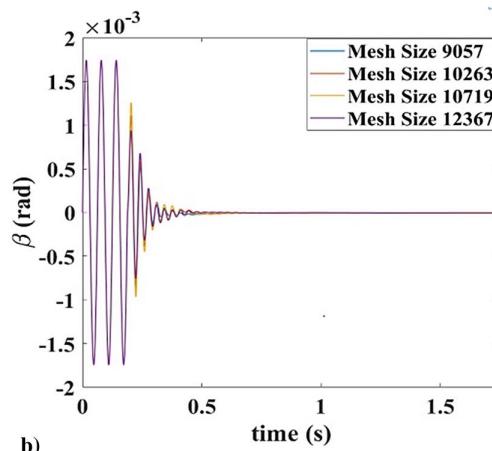


Fig. 11 Limit cycle oscillation of the aileron at M_∞ of 0.86 at angle of attack of 2 deg for viscous flowfield.

approximation of linear dynamics gives reasonable accuracy. At a freestream M_∞ of 0.7, the flow physics can be explained by the linearized dynamics about the steady state due to the absence of nonlinearities such as flow separation and strong shock interaction. The subspace-identification-based linearized ROM is first trained by the input gust signal shown in Fig. 12a, and then the same input signal is used for the prediction of the lift coefficient C_l response, which is then compared with the corresponding response from the high-fidelity CFD simulation. Figure 12b shows that the prediction of the lift coefficient response from the high-fidelity CFD simulation and the linear reduced-order model appear to match well. Although the linearized ROM has been demonstrated to yield very effective predictions of the transonic gust response of the airfoil at the lower spectrum of the transonic regime, this may not be the case for a higher transonic M_∞ of 0.854, which causes flow separation at the foot of the shock front. The prediction of the transonic gust response of the airfoil at this transonic Mach number corresponding to the same gust velocity input signal shown in Fig. 7a indicates that the linearized ROM fails to capture the unsteady transonic gust response of the airfoil at M_∞ of 0.854. Figure 13a shows the linear ROM prediction of the gust response of the airfoil (i.e., the variation of the lift coefficient) deviating considerably in comparison with that predicted from the CFD simulations. Similarly, one could also compare the linear ROM prediction of the hinge moment coefficient resulting from the training structural input signal corresponding to the aileron movement (i.e., Fig. 9a) with the high-fidelity CFD simulation of the aileron buzz in Fig. 13b in a freestream M_∞ of 0.854 and a Re of 10^7 . Here, again, it can be seen that the predicted result from linear ROM does not match well with the predictions from the CFD simulations.

The inability of the linear ROM in reconstructing the training signal at higher Mach numbers at which flow separation occurs at



Downloaded by ISAE on April 29, 2021 | http://arc.aiaa.org | DOI: 10.2514/1.J059027

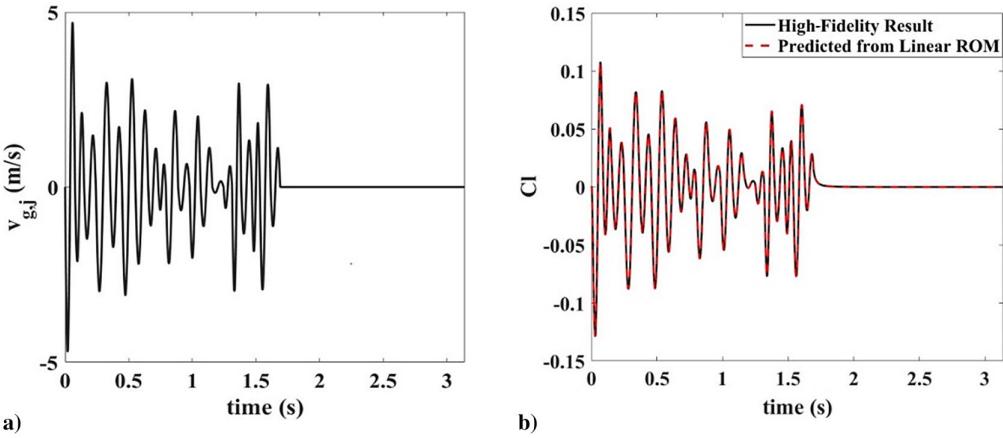


Fig. 12 a) Input gust velocity signal for the airfoil in a transonic flow at M_{∞} of 0.7 and Re of 10^7 and b) comparing lift coefficient response predicted using linearized ROM with that from CFD simulation.

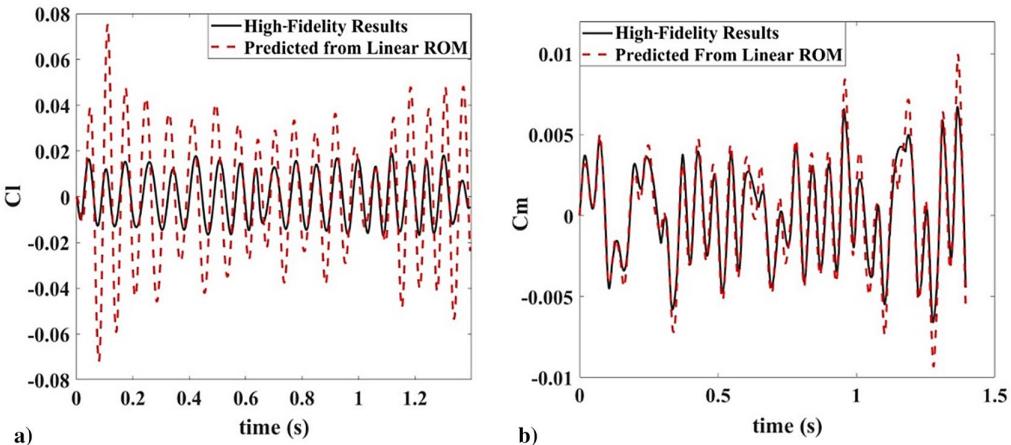


Fig. 13 The comparison of (a) lift coefficient responses subjected to input gust velocity signal shown in Figs. 7a and (b) moment coefficient subjected to structural input signal shown in Fig. 9a predicted using linearized ROM and CFD simulation corresponding to a transonic flow at M_{∞} of 0.854 and Re of 10^7 .

the foot of the shock front guarantees the ineffectiveness of linear ROM approach even for different input signals other than the training signal used here. The limitation of linear ROM predictions at higher transonic Mach numbers can be overcome by using a nonlinear ROM via a deep-learning approach. In this section, only the global forces are reconstructed effectively using the linear ROM at the lower transonic regime. The distributive variables like the pressure coefficient and skin friction coefficient distribution over the airfoil or the Mach or the pressure contours in the entire computational domain does not follow linear dynamics even at the lower transonic regime because of the presence of the discontinuity in the solution space, and hence the linear ROM is a poor choice for the unsteady distributive variable reconstruction under the gust or structural input excitation of significantly large amplitude. In the following section, the non-linear output responses of the local flow variables under the action of sinusoidal and arbitrary gust input consisting of a combination of sinusoidal and one minus cosine signals and sinusoidal structural input are addressed.

C. Nonlinear-ROM-Based LSTM Deep-Learning Network Approach

The potential and viability of using a nonlinear ROM based on the LSTM network and DEIM algorithm coupled with an LSTM network named DEIM-LSTM ROM as proposed in Sec. III for predicting nonlinear unsteady transonic flowfield are demonstrated in this section for several problems involving transonic airfoil-gust response and aileron buzz.

1. Predicting Nonlinear Transonic Airfoil-Gust Response

The LSTM network is first used for the reconstruction of transonic airfoil-gust response at M_{∞} of 0.854 and Re of 10^7 . First, the LSTM network consisting of four hidden layers and 50 neurons in each hidden layer is trained with the input signal shown in Fig. 7a and the corresponding Cl and Cm output computed using CFD for this training signal. The last layer contains one neuron as it is linked with one global coefficient Cl or Cm response. The hyperbolic tan,

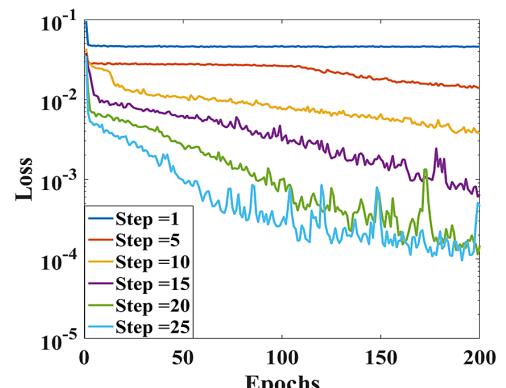


Fig. 14 Loss function vs iteration in the LSTM network (epochs) for different step size choices during training.

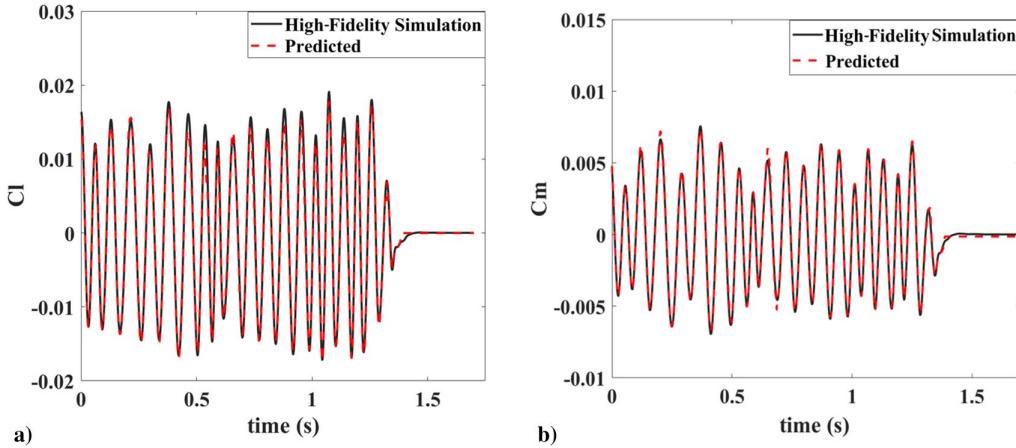


Fig. 15 Comparison of a) Cl and b) Cm coefficients predicted using LSTM network coupled with DEIM algorithm with that predicted using CFD for the gust response of airfoil in a transonic flow at M_∞ of 0.854 and Re of 10^7 subjected to input gust velocity signal similar to that shown in Fig. 7a.

i.e., (\tanh), activation function is used for the generation of hypersurfaces to form the functional relationship between the gust input and the global aerodynamic lift and moment coefficients. The step size discussed in Sec. III is estimated as 25. A comparative study on the corresponding loss function with the number of epochs (number of iterations in ADAM optimizer) is shown in Fig. 14. If the step size is considered less than 5, the loss function hits a local minimum and does not decay further, whereas if the step size is increased to 25, the loss function starts to decay and reach a global minimum with effective learning of the functional relationship between the input and output. For the global coefficient, the LSTM network is enough to reconstruct the unsteady variables and does not require coupling with the DEIM-based interpolation approach. Figures 15a and 15b compares the Cl and Cm response between the high-fidelity CFD-based result and the predicted result from the LSTM network under

the action of the training gust input signal shown in Fig. 7a. For the same flow conditions, the trained LSTM approach is used for the reconstruction of a sinusoidal gust input to assess the effectiveness of the trained network in making predictions to arbitrary gust input signals. The sinusoidal gust input signal which has an amplitude of 1 m/s, length λ of 25, and period n of 20 is fed as input to the trained LSTM network as demonstrated in Fig. 16a. Figures 16b and 16c compare the variation of lift and moment coefficients Cl and Cm predicted by the trained network with the predictions from the high-fidelity CFD simulations for the same signal. The detail discussion behind the choice of the neurons and hidden layers is discussed in a separate section in Supplemental Material SM3.

Figures 17a and 17b show complex training and the test signal which consist of the sine and one minus cosine signal. Figures 17c and 17d demonstrate that the ROM matches significantly well with

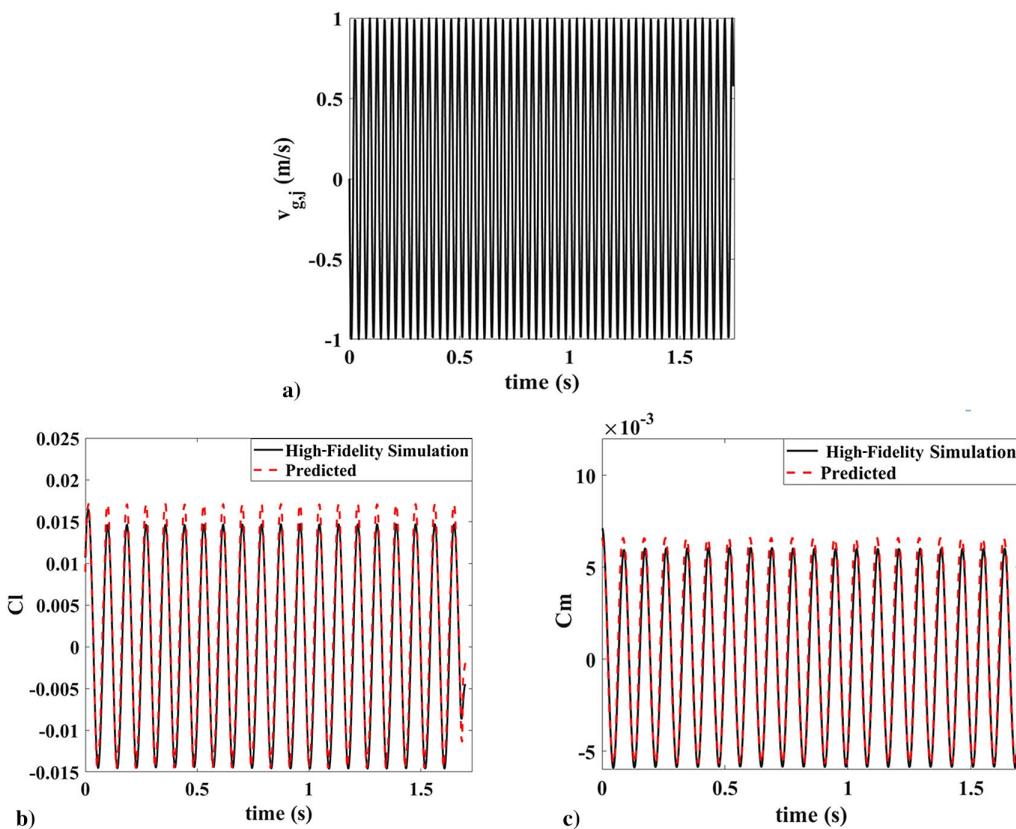


Fig. 16 (a) The profile of the input test gust velocity signal consisting of a train of sinusoidal gusts to the aeroelastic system and the comparison of the responses of b) Cl and c) Cm predicted using the LSTM network with the corresponding responses predicted using CFD for a transonic flow at M_∞ of 0.854 and Re of 10^7 .

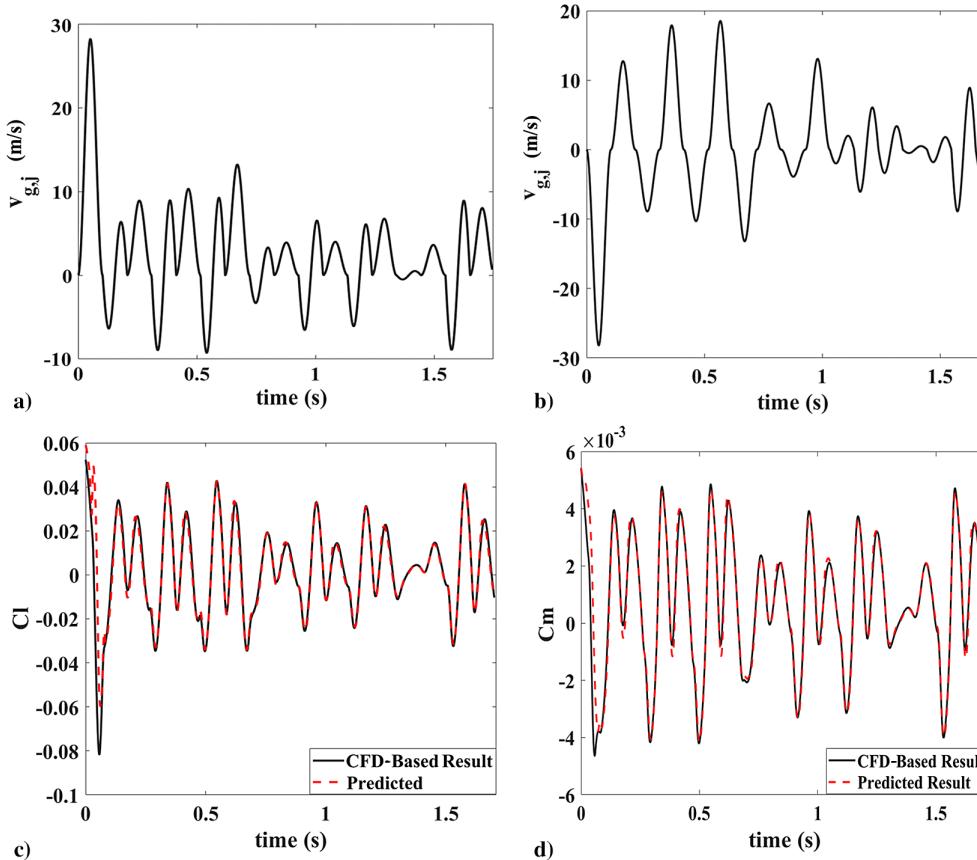


Fig. 17 Complex a) training and b) test signal consisting of the sine and one minus cosine signal of different amplitudes. Comparison of c) C_l coefficient and d) C_m coefficient of test signal between high-fidelity CFD based result and the predicted results.

the C_l and C_m coefficient (about the three-quarters of the chord length) response from the high-fidelity CFD-based results. In this case, four hidden layers and 150 neurons in each layer are used.

2. Reconstruction of Distributive Forces on Airfoil Surface During Gust Interaction

The LSTM network is now trained to achieve the reconstruction of distributive forces such as the ΔC_p and ΔC_f distribution on the airfoil. First, a steady-state flowfield at M_∞ of 0.854 and Re of 10^7 is generated. Then, the steady-state aerodynamic field is excited with the training gust input signal shown in Fig. 7a. The DEIM algorithm is applied on the dataset D containing the ΔC_p and ΔC_f distribution $D \in \mathbb{R}^{N \times n_t}$, where N is the surface grid location and the n_t is the total number of snapshots. An error analysis for the choice of the number of DEIM modes is considered by measuring the relative L2 error, i.e.,

$\sqrt{\sum (y_{\text{predicted}} - y_{\text{truth}})^2} / \sqrt{\sum (y_{\text{truth}})^2}$, where $y_{\text{predicted}}$ and y_{truth} are the predicted and actual values of the expected value of the output or response. The relative L2 error is estimated for both ΔC_p and ΔC_f at the end of the 424th time step (an arbitrary point is chosen) of the training signal corresponding to ΔC_p and ΔC_f , and it reduces to approximately 1 and 2%, respectively, from approximately 4 and 8% when the DEIM modes are increased from 8 modes to 15 modes. Therefore, 15 modes are chosen for the reconstruction of the distributive variables, and this number is kept the same for all the remaining experiments. The singular values are obtained by applying the singular value decomposition (SVD) on the training dataset D as shown in Fig. 18. It is clear from the singular value plot that most of the energy is contained in the first 15 modes and the singular values (\sim measure of the energy contained in the dynamical system) drops to $\sim 10^{-3}$ within the selected DEIM modes. The singular values are normalized with the largest or the first entry in the singular value matrix after the application of SVD.

The corresponding DEIM control point locations on the airfoil surface for the prediction of the ΔC_p and ΔC_f distribution are shown

in Figs. 19a and 19b. The number of the surface mesh distribution is considered as 200, resulting in the size of the output in the LSTM network being reduced from $\mathbb{R}^{200 \times n_t}$ to $\mathbb{R}^{15 \times n_t}$, where n_t is the signal length. The majority of DEIM control points are distributed mostly near the shock and trailing edge because these locations are undergoing maximum changes for unsteady dynamics. The supersonic regime over the airfoil follows comparatively linear dynamics as compared to those near the shock and near the circulation dominated trailing edge with the change in gust velocity input; therefore, a few numbers of control points would be able to reconstruct the supersonic pocket over the airfoil. Figure 19a shows only one point for the ΔC_p distribution and Fig. 19b shows two points located in the vicinity of the supersonic pocket for the ΔC_f distribution.

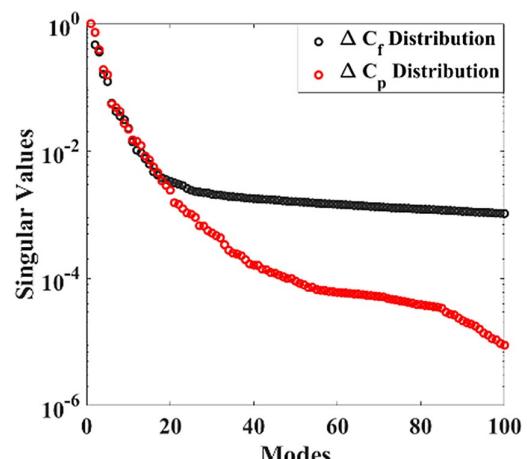


Fig. 18 Singular value plots of the dataset D containing the ΔC_p and ΔC_f distribution under the training signal proposed in Fig. 7a.

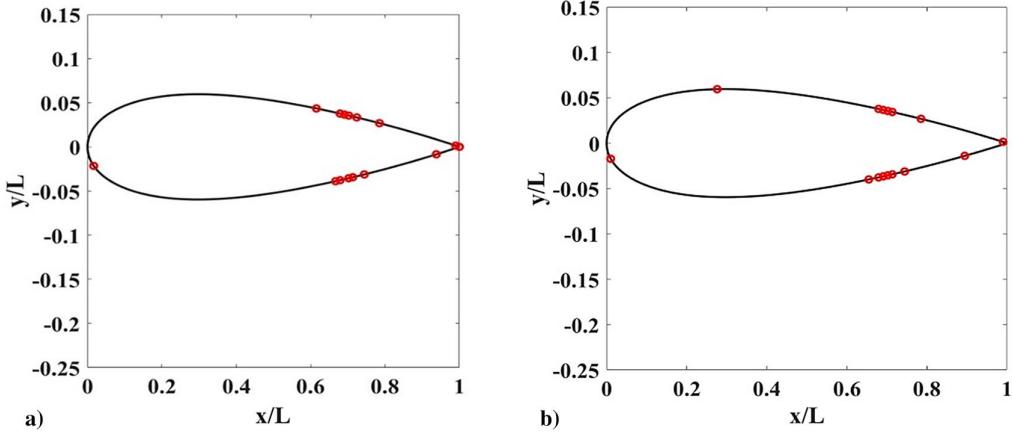


Fig. 19 DEIM control point locations for a) ΔC_p distribution and b) for ΔC_f distribution.

The trained nonlinear ROM, DEIM-LSTM network is then used for the reconstruction of the distributive variables ΔC_p and ΔC_f distribution corresponding to a gust signal which is completely different from the input signal used for training the network. The sinusoidal gust input used for the reconstruction of the global lift and moment coefficients earlier is used here for the reconstruction of the distributive variables. The variations of ΔC_p and ΔC_f under the sinusoidal excitation are shown in the Supplemental Material in Figs. S8 and S9, demonstrating the nonlinear flow features at first six DEIM control points. The close match of the predicted ΔC_p and ΔC_f distribution with the high-fidelity simulation shown in Figs. S6 and S7 ensure the full ΔC_p or ΔC_f reconstruction at any time steps after multiplication with the DEIM modes ϕ .

The predicted ΔC_p and ΔC_f distribution on the upper and lower surfaces of the airfoil at the highest positive amplitude location corresponding to this input signal are shown and compared with the high-fidelity CFD prediction in Fig. 20. The positive value of the ΔC_f distribution in the lower surface shown in Fig. 20c, and the positive value of the ΔC_f distribution in the upper surface demonstrated in Fig. 20b shows the occurrence of flow separation at this particular M_∞ .

The corresponding relative L2 error percentage for variables ΔC_p and ΔC_f at the maximum positive amplitude location and over a periodic cycle is shown in Table 1. The difference between the upper and lower surface error distributions is due to the different shock positions leading to different shock-boundary-layer dynamics on these two surfaces.

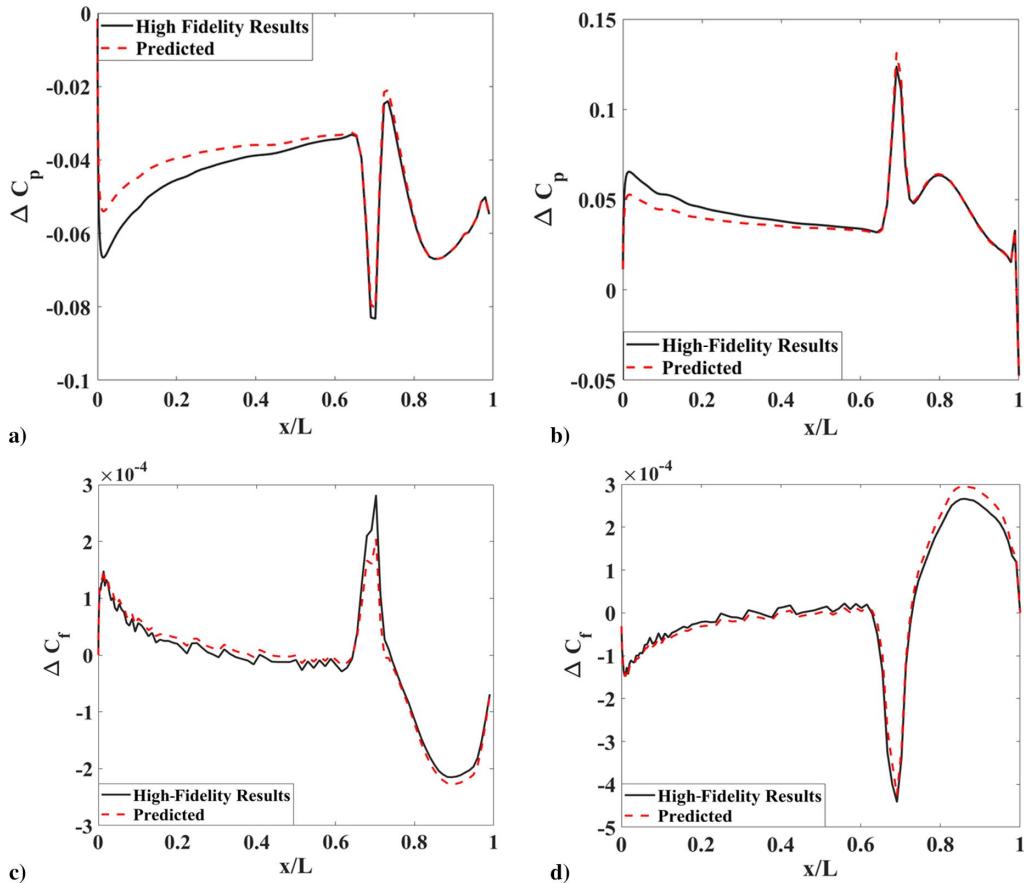


Fig. 20 ΔC_p distribution on the (a) lower surface and (b) upper surface of the airfoil. ΔC_f distribution in the (c) lower and (d) on the upper surface of the airfoil corresponding to the transonic gust response of airfoil in a transonic flow at M_∞ of 0.854 and Re of 10^7 subjected to sinusoidal gust input.

Table 1 L2 error percentage corresponding to the sinusoidal gust excitation

Distribution	Error, %
<i>L2 error at the maximum positive amplitude location</i>	
ΔC_p in upper surface	12.0051
ΔC_p in lower surface	11.8258
ΔC_f in upper surface	12.5570
ΔC_f in lower surface	15.0128
<i>L2 error over an entire periodic cycle</i>	
ΔC_p in upper surface	16.5898
ΔC_p in lower surface	15.6496
ΔC_f in upper surface	12.2132
ΔC_f in lower surface	15.9991

3. Reconstruction of Unsteady Transonic-Airfoil Gust Response Flowfields

The nonlinear DEIM-LSTM network algorithm can be applied for the reconstruction of the full unsteady flowfield, and this is demonstrated by keeping the LSTM hyperparameters and the number of DEIM modes the same as those for the ΔC_p and ΔC_f distribution. The training signal considered here consists of 1000 time steps. The computational domain contains 33,245 cell locations; therefore, the size of the output channel is decreased from $\mathbb{R}^{33245 \times n_t}$ to $\mathbb{R}^{15 \times n_t}$ after the application of the DEIM algorithm on the full flowfield data computed using CFD. Figure 21 shows the actual and reconstructed Mach contours at M_∞ of 0.854 and Re of 10^7 at the numerical time step corresponding to the maximum positive amplitude location since the train of sinusoidal gust load encounters the leading edge of the airfoil. Figure 21a shows the actual unsteady Mach contour considering high-fidelity CFD-based result, whereas Fig. 21b shows the reconstructed Mach contour using the proposed DEIM-LSTM approach. It is evident from Fig. 21 the proposed

DEIM-LSTM ROM has been very effective in the reconstruction of the flow contours in the entire computational domain despite the presence of the nonlinearity in the flowfield arising from the circulation due to adverse pressure gradient at the foot of the shock wave. The absolute error distribution is demonstrated in Fig. 21c. The first four DEIM modes are shown in Fig. 22. The singular value distribution shown in Fig. 23 demonstrates that the first 15 modes here as well contain most of the energy of the dynamical system. Although the singular values have not decayed as fast as the ΔC_p and ΔC_f distribution over the airfoil, the reconstructed flowfield has matched well with the high-fidelity simulation.

The corresponding distribution of the DEIM control point locations distributed in the entire flow domain is shown in Fig. 23. The distribution of the DEIM control points to enable the reconstruction is located near the shock front because the flow structures at these points are the ones mostly affected due to the unsteadiness induced by the gust front movement.

4. Prediction of Transonic Aileron Buzz

A typical input training signal for the structural excitation β shown in Fig. 9a is generated to contain all the necessary frequency components for a transonic aileron-buzz motion and the Fast Fourier Transform (FFT) of this training signal shown in Fig. 24 indicates that the signal has a frequency in the range of 0–200 rad/s and the x -axis showing the frequency is expressed in a logarithmic scale. All the hyperparameters of the nonlinear DEIM-LSTM network are kept at the same values as those used for the prediction of the transonic airfoil-gust prediction. The network is trained with this structural input, and the corresponding variation of the hinge moment coefficient Cm_z is predicted from the network and compared with the corresponding CFD prediction in Fig. 25a. Similarly, Fig. 25b shows the predicted variation of the hinge moment coefficient Cm for a sinusoidal structural excitation β of 2 deg $\sin(100t)$ of the aileron attached to the airfoil immersed in a transonic flow at M_∞ of 0.854 and Re of 10^7 and compares this with that predicted from CFD.

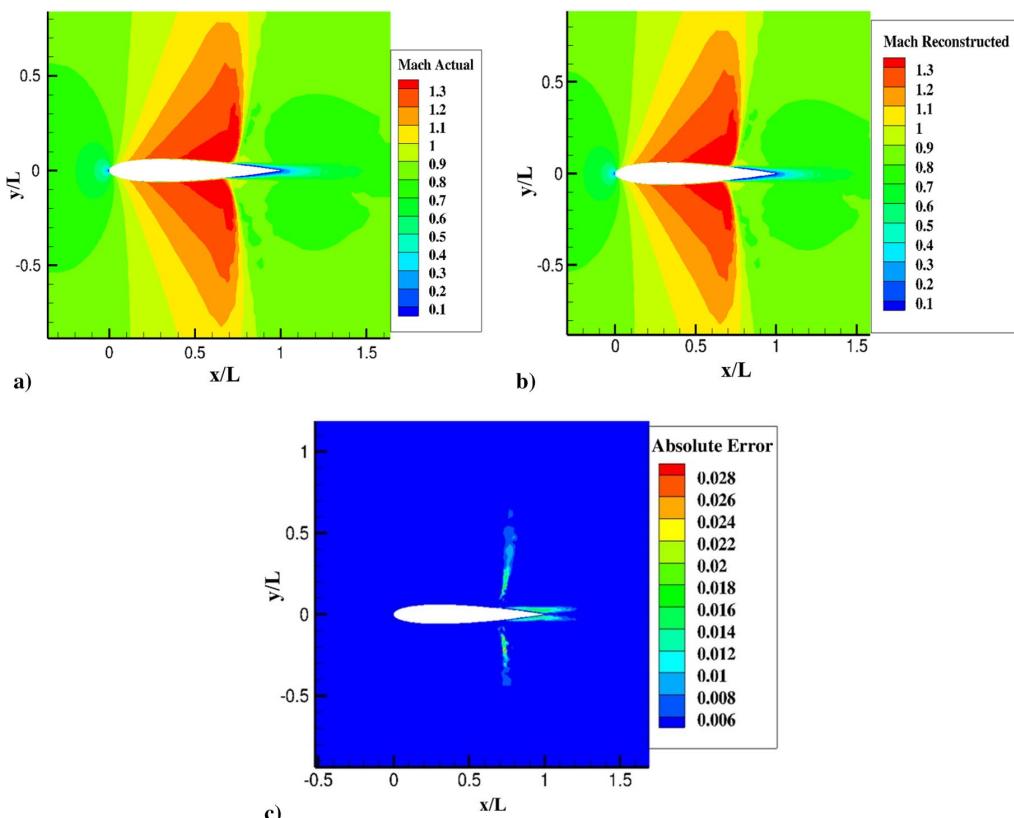


Fig. 21 a) Actual and b) reconstructed Mach contours in the flow domain at the maximum positive input location of the sinusoidal gust signal and c) absolute error corresponding to the transonic gust response of airfoil in a transonic flow at M_∞ of 0.854 and Re of 10^7 .

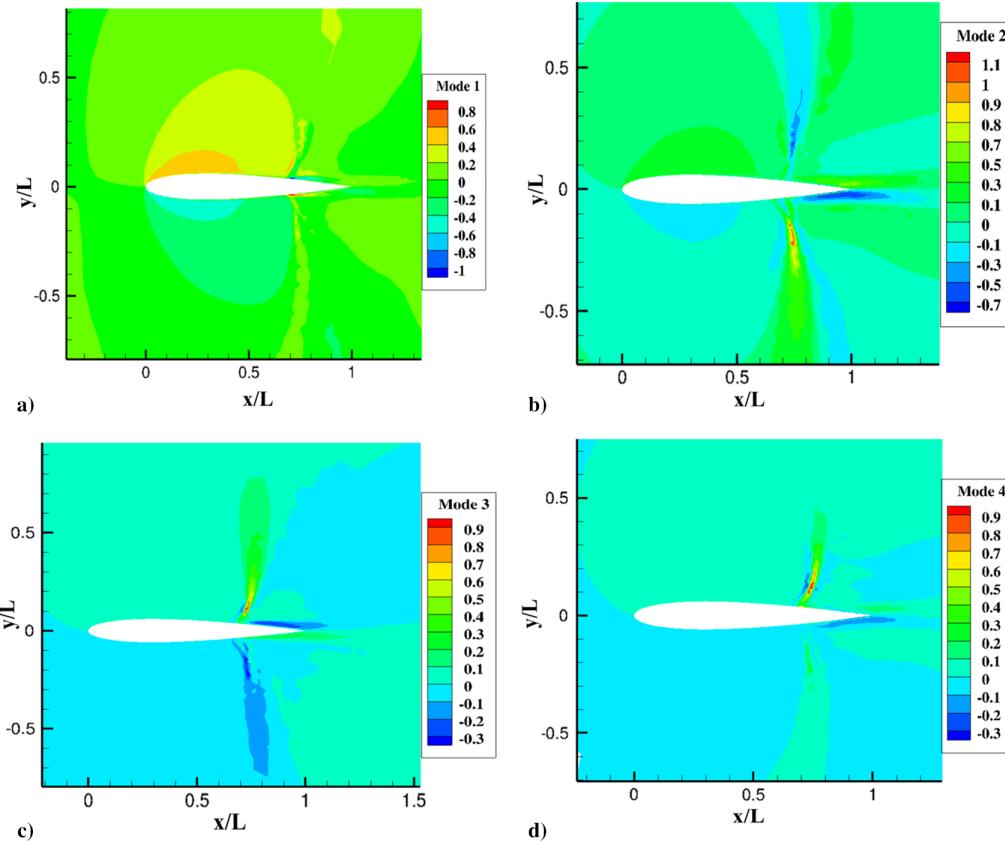


Fig. 22 First four DEIM modes corresponding to a) mode I, b) mode II, c) mode III, and d) mode IV of the Mach contours affected by the gust load corresponding to the gust response of airfoil in a transonic flow at M_{∞} of 0.854 and Re of 10^7 under the excitation of the training gust input.

The global lift and moment coefficients have matched significantly well with the high-fidelity simulation subjected to training and test signals attesting the robustness of current ROM algorithm for structural input as well. For the distributive variable reconstruction, the DEIM-LSTM network needs to be applied similar to the previous test case. Fifteen DEIM modes are considered for using the nonlinear ROM for the reconstruction of the distributive variables of interest, i.e., ΔC_p and ΔC_f distribution at the maximum amplitude locations corresponding to a sinusoidal structural excitation of $2 \text{ deg} \sin(100t)$. The number of modes here as well is decided considering an error analysis and singular value plots like airfoil-gust interaction.

Figures 26a–26d compare the distributive variables at the lower and upper surfaces of the airfoil from nonlinear DEIM-LSTM network predictions with the corresponding predictions from CFD simulations. The ΔC_p distribution demonstrated in Figs. 26a and 26b shows a peak near the shock, and the ΔC_f distribution shown in

Figs. 26c and 26d for the lower surface attains a positive hump, and the upper surface attains a negative hump near the foot of the shock due to flow separation effect.

The DEIM control points are mostly scattered near the shock location and trailing edge to capture the unsteady shock boundary-layer dynamics leaving only one control point near the supersonic pocket for the ΔC_p distribution in Fig. 27a and none for the ΔC_f distribution shown in Fig. 27b.

Table 2 shows the L2 error percentage corresponding to the maximum positive amplitude location of the sinusoidal test excitation and error over a periodic cycle.

From the error distribution, it is clear that the ΔC_p distribution shows a better agreement with that predicted from CFD as opposed to the ΔC_f distribution. The L2 error is higher for the airfoil-gust response as compared to the structural interaction. This error can be minimized by improving the training signal with more variations of λ and $v_{g,o}$ of the gust excitation. Similarly, the unsteady flowfield

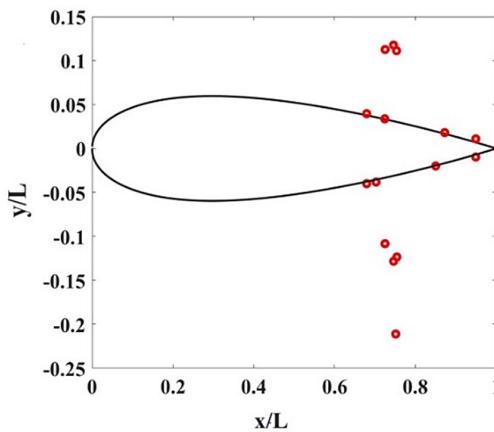


Fig. 23 Distribution of DEIM control points for the gust input excitation over the entire flowfield.

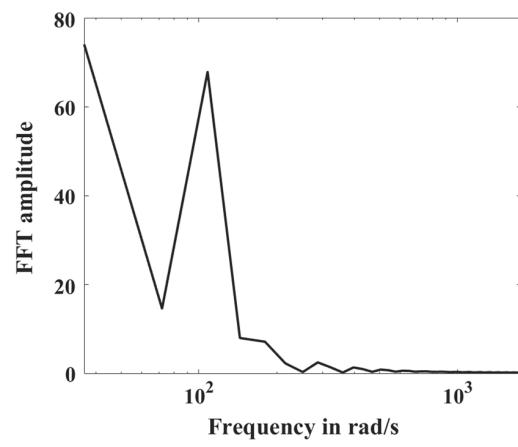


Fig. 24 FFT amplitude on the training structural input.

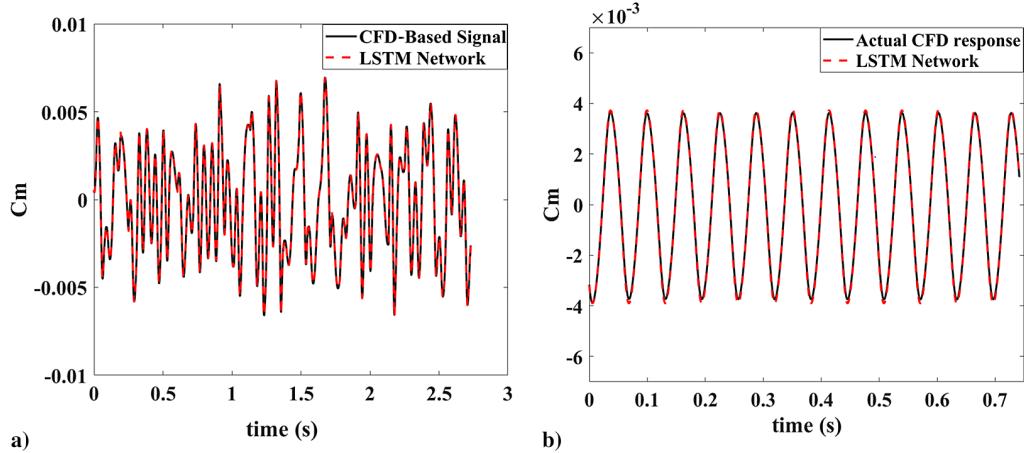


Fig. 25 Comparison of C_m using LSTM network and CFD-based result under a) training signal and b) sinusoidal input in viscous flowfield assumption.

can be reconstructed at the maximum amplitude locations corresponding to a sinusoidal structural excitation of β at 2 deg $\sin(100t)$ using DEIM, and this reconstruction of the signal is shown and compared with the unsteady flowfield computed by CFD at the same instant is shown in Fig. 28.

The DEIM control points are scattered near the shock location and the training edge even for the full flowfield prediction as demonstrated in Fig. 29. The proximity of all the DEIM points is close to the airfoil, and no single point being placed near the farfield is due to the fact that the steady-state contour gets subtracted from the unsteady flowfield; therefore, the flow structure remains same away from the airfoil even with the structural interaction.

5. Combined Structural and Gust interaction

This section discusses the reconstruction of the unsteady global coefficients under the action of both sinusoidal gust input and the sinusoidal structural response at the M_∞ of 0.854 and Re of 10^7 . The linear superposition of structural response and the gust interaction gives a reasonably good prediction for the combined gust and structural response, as demonstrated by Raveh [12] if nonlinearity of the flowfield is not extreme. To enhance the nonlinearity of the flow physics and attest the robustness of the current LSTM based approach for accounting the nonlinear gust structural interaction, the scalar magnitude of the training and sinusoidal gust input signal considered

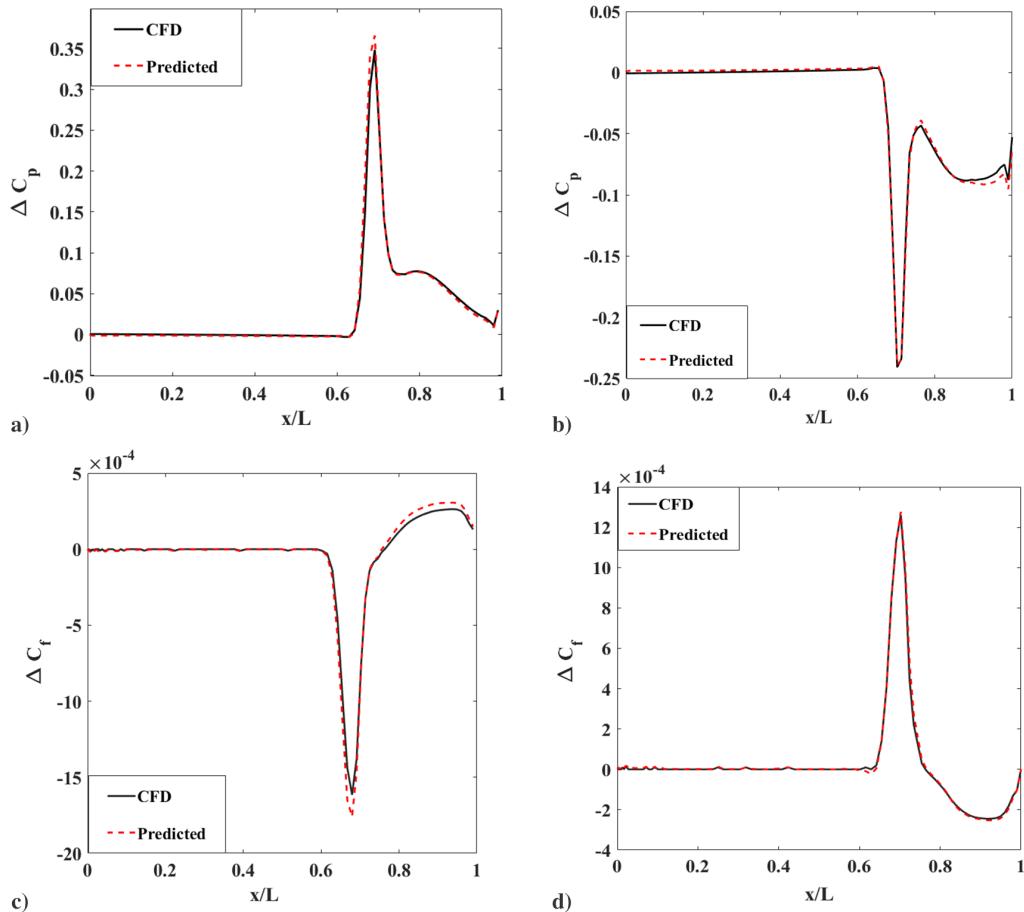


Fig. 26 Comparison of the ROM prediction of a) lower surface ΔC_p distribution, b) upper surface ΔC_p distribution, c) lower surface ΔC_f distribution, and d) upper surface ΔC_f distribution with the corresponding CFD predictions for sinusoidal aileron motion at M_∞ of 0.854 and Re of 10^7 .

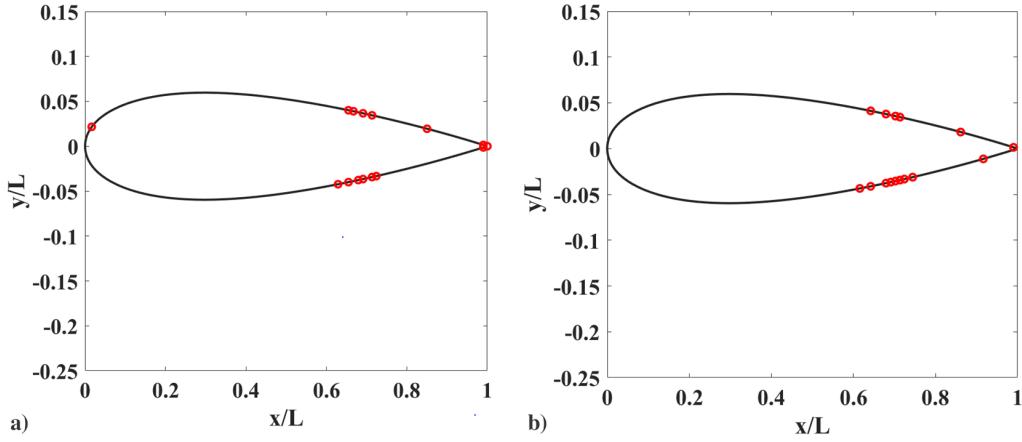


Fig. 27 Grid locations for a) ΔC_p distribution and b) ΔC_f distribution.

Table 2 L2 error percentage corresponding to the sinusoidal aileron excitation

Distribution	Error, %
<i>L2 error at the maximum positive amplitude location</i>	
ΔC_p in upper surface	5.2587
ΔC_p in lower surface	9.6352
ΔC_f in upper surface	5.5600
ΔC_f in lower surface	12.8179
<i>L2 error over an entire periodic cycle for aileron buzz</i>	
ΔC_p in upper surface	4.910
ΔC_p in lower surface	4.862
ΔC_f in upper surface	8.359
ΔC_f in lower surface	7.143

in previous test cases are multiplied with a factor of 5. The training and test input signal corresponding to the structural interaction is kept similar. The training and test sinusoidal input for the structural interaction are kept same. Figure 30 shows the combined gust structural interaction under the sinusoidal gust and structural input and matched with the CFD-based high-fidelity simulation. The gust response induces different phase lag and amplitude in the aerodynamical system as compared to the structural input, and therefore the combined response has shown nonperiodic oscillation even after sinusoidal excitation from both the gust and structural input.

Table 3 shows the approximate time duration for the different test cases considered in the present work. The wall clock time mentioned here corresponds to the training signal length of 1000 and the sinusoidal test signal of 500.

For the airfoil–gust and airfoil–structural interaction, the training time for the LSTM and the DEIM–LSTM network is almost the same

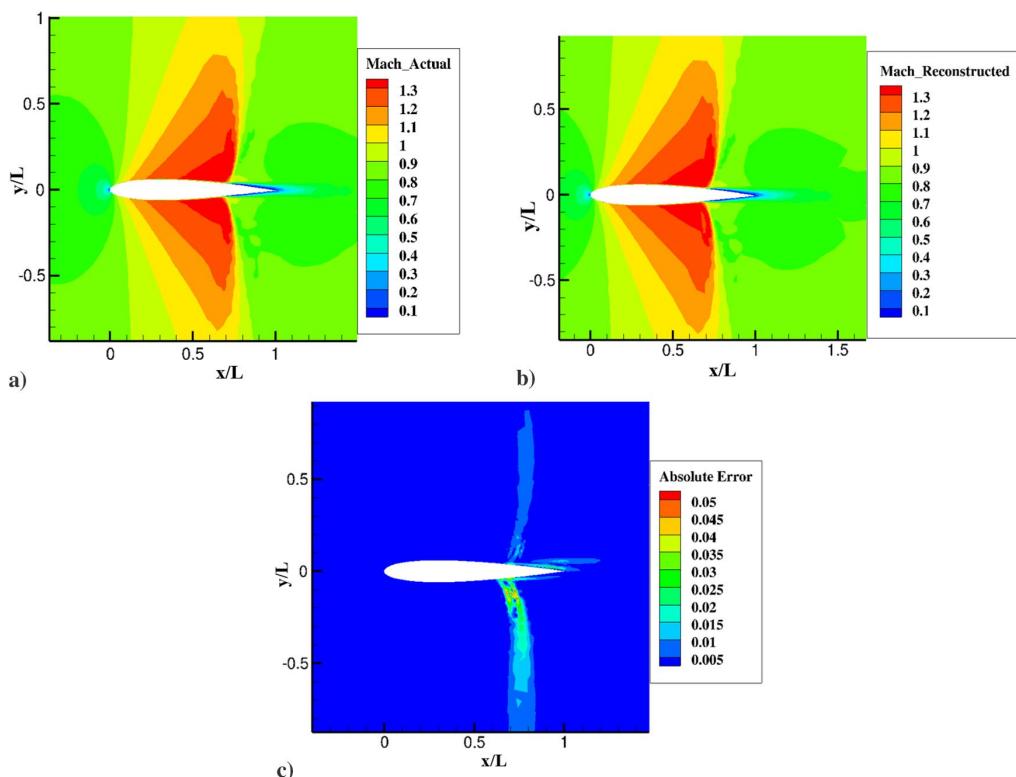


Fig. 28 a) Actual and b) reconstructed Mach contours in the flow domain at the maximum positive input location of the sinusoidal structural input and c) absolute error corresponding to the structural interaction of airfoil in a transonic flow at M_∞ of 0.854 and Re of 10^7 .

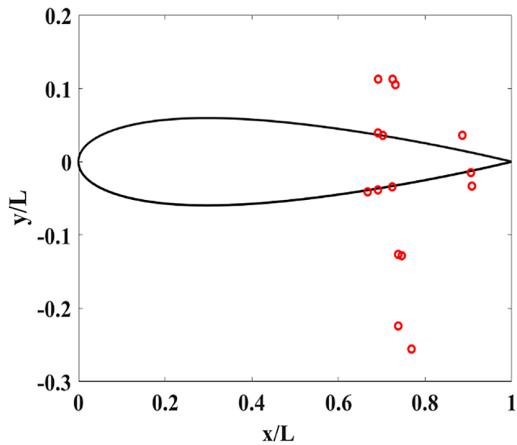


Fig. 29 Distribution of DEIM control points over the entire flowfield for the structural excitation to the aerodynamic system.

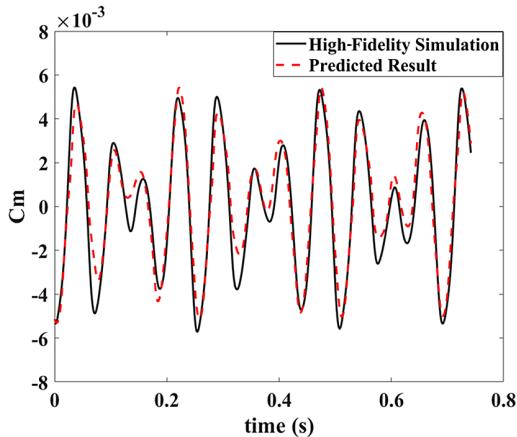


Fig. 30 Combined gust and structural response under sinusoidal input at M_{∞} of 0.854 and Re of 10^7 .

because of the data-driven nature of the current work. It means that, irrespective of the test cases, as long the size of the data remains the same, the wall clock times almost match with each other. The input size gets doubled for the combined gust structural interaction and thereby increases the time taken for the training of global coefficients for the combined problem. The high-fidelity CFD-based simulations are carried out in a 12-core high-performance parallel computation framework. The computational time corresponding to different problems of interest differs due to the variation in the convergence rate at each global time step. The LSTM training and MATLAB® operation of the DEIM algorithm is carried out on a Lenovo laptop with a dual-core i7 processor, clock speed of 2.4 GHz, and 8 GB RAM. The time taken for the DEIM control point and DEIM modes computation is insignificant ($\sim 1\text{--}5$ s) as compared to the LSTM training; therefore, the training time shown in Table 3 excludes the time taken for the DEIM algorithm for the distributive variable reconstruction.

Table 3 Approximate time duration of different tests and training signal computation in CFD and LSTM network

Response	Training signal generation (CFD), min	Global coefficient training (LSTM), min	Distributed variable training (DEIM-LSTM), min	Test signal generation (CFD), min
Airfoil gust	488	17	9	229
Airfoil-structural	312	18	8	199
Combined gust-structural	465	17		220

V. Conclusions

The current work focuses on the impact of different inputs like gust and structural interaction on the aerodynamic system and proposes a deep-learning-based nonlinear ROM. First, This work explores the physics involved with the continuous gust interaction with a rigid airfoil and then classical aileron buzz. The current work proposes a reduced-order computational approach which will account for these nonlinear aerodynamic interactions with structural and gust input leveraging the huge computational cost (at least one order less) of the high-fidelity CFD-based simulation. It first applies the linear ROM for both the structural and gust input and shows its limitation only at the lower Mach regime. The flow-separation effect makes the linear ROM poor machinery for the prediction of the global and distributive variable at a transonic regime near Mach number of 0.85. Then, an LSTM deep-learning network-based ROM is adopted for the reconstruction of the global coefficients under the excitation of gust, structural or combined input. The global load and moment coefficient reconstruction in case of structural input has performed better than reconstruction under gust input. Here, it is shown that if a test function consists of a more complex signal like a combination of sinusoidal and one minus cosine functions, the training signal also needs to be rich in similar complex functions. The current LSTM algorithm is further coupled with the DEIM algorithm to reconstruct the distributive variables. The effect of the number of DEIM modes on the reconstruction part and the effect of step size in the LSTM network for achieving a reliable network is studied in the current work. The relative L2 error shows that the accuracy of reconstruction of the distributive variable lies inside an acceptable accuracy. The supersonic regime over the airfoil is comparatively linear compared to those near the shock and near the circulation dominated trailing edge with the change in gust velocity input; therefore, a few numbers of DEIM control points can reconstruct the supersonic pocket over the airfoil. The prediction of the distributive variable under the structural excitation has been more effective (L2 error less than 10%) as compared to the prediction of the distributive variable under the gust load excitation (L2 error $\sim 10\text{--}20\%$). Suitable design of the training signal and hyperparameter tuning may reduce the error limit corresponding to the gust input excitation. The aileron motion is generally controlled in the commercial aircraft for the gust load alleviation. The current work proposes a computationally effective platform for the quick prediction of aerodynamic forces due to the structural interaction and continuous gust load on an airfoil leading to a possible way of designing a controller for gust load by manipulating the aileron motions.

References

- [1] US Dept. of Transport, "Federal Aviation Authority (FAA): Title 14, Code of Federal Regulations (14 CFR) 25.341," Gust and Turbulence loads, Advisory Circular No. AC250341-1, Dec. 2014, https://www.faa.gov/documentLibrary/media/Advisory_Circular/AC_25_341-1.pdf.
- [2] Albano, E., and Rodden, W. P., "A Doublet Lattice Method for Calculating Lift Distribution on Oscillating Surfaces in Subsonic Flow," *AIAA Journal*, Vol. 7, No. 2, Feb. 1969, pp. 279–285.
- [3] Sitaraman, J., and Baeder, J. D., "Field Velocity Approach and Geometric Conservation Laws for Unsteady Flow Simulations," *AIAA Journal*, Vol. 44, No. 9, Sept. 2006, pp. 2084–2094.
- [4] Wales, C., Jones, D., and Gaitonde, A., "Reduced Order Modelling for Aeroelastic Aerofoil Response to a Gust," *Proceedings of 51st AIAA Aerospace Sciences Meeting Including the New Horizons Forum and Aerospace Exposition*, AIAA Paper 2013-0790, Jan. 2013.
- [5] Lambourne, N. C., "Control-Surface Buzz," Aeronautical Research Council R&M 3364, London, England, U.K., May 1962.
- [6] Erickson, A. L., and Stephenson, J. D., "A Suggested Method of Analysing for Transonic Flutter of Control Surfaces Based on Available Experimental Evidence," NACA Research Memorandum A7F30, 1947.
- [7] Steger, J. L., and Bailey, H. E., "Calculation of Transonic Aileron Buzz," *AIAA Journal*, Vol. 18, No. 3, March 1980, pp. 79–134.
- [8] Bendiksen, O. O., "Non-Classical Aileron Buzz in Transonic Flow," *Proceedings of 34th AIAA Structures, Structural Dynamics and Materials Conference*, AIAA Paper 1993-1479, April 1993.

- [9] Bendiksen, O. O., "Influence of Shock on Transonic Flutter of Flexible Wings," *Proceedings of the 50th AIAA/ASME/ASCE/AHS/ASC, Structures, Structural Dynamics and Materials Conference*, AIAA Paper 2009-2313, May 2009.
- [10] Rampurawala, A. M., "Aeroelastic Analysis of Aircraft with Control Surfaces Using CFD," Ph.D. Dissertation, Univ. of Glasgow, Glasgow, Scotland, 2006.
- [11] Raveh, D., "CFD-Based Models of Aerodynamic Gust Response," *Proceedings of 47th AIAA/ASME/AHS/ASC Structures, Structural Dynamics, and Materials Conference*, AIAA Paper 2006-2022, May 2006.
- [12] Raveh, D., "Gust Response Analysis of Free Elastic Aircraft in the Transonic Flight Regime," *Journal of Aircraft*, Vol. 48, No. 4, May 2012, pp. 1204–1222.
- [13] Ghoreyshi, M., Greisz, I., Jirasek, A., and Satchell, M., "Simulation and Modelling of Rigid Aircraft Aerodynamic Responses to Arbitrary Gust Distributions," *Aerospace*, Vol. 43, No. 5, April 2018, pp. 2084–2094.
- [14] Williams, S.P. I., Jones, D. P., Gaitonde, A. L., Wales, C., and Huntley, S. J., "Application of Reduced Order Models in Aircraft Gust Response Studies," *Proceedings of 46th AIAA Fluid Dynamics Conference*, AIAA Paper 2016-4261, June 2016.
- [15] Timme, S., Badcock, K. J., and Ronch, A. D., "Linear Reduced Order Modelling for Gust Response Analysis Using the DLR-TAU Code," *Proceedings of International Forum on Aeroelasticity and Structural Dynamics*, IFASD-2013-36A, Bristol, United Kingdom, June 2013.
- [16] Bekemeyer, P., Ripepi, M., Heinrich, R., and Gortz, S., "Nonlinear Unsteady Reduced Order Models Based on Computational Fluid Dynamics for Gust Loads Predictions," *Proceedings of Applied Aerodynamics Conference*, AIAA Paper 2018-3635, June 2018.
- [17] Schmidhuber, J., "Deep Learning in Neural Networks: An Overview," *Neural Networks*, Vol. 61, No. 1, 2015, pp. 85–117.
- [18] Brunton, S. L., Noack, B. R., and Koumoutsakos, P., "Machine Learning for Fluid Mechanics," *Annual Review of Fluid Mechanics*, Vol. 52, No. 1, Jan. 2020, pp. 477–508.
- [19] Parish, E. J., and Duraisamy, K., "A Paradigm for Data-Driven Predictive Modeling Using Field Inversion and Machine Learning," *Journal of Computational Physics*, Vol. 305, No. 1, Jan. 2016, pp. 758–774.
- [20] Maulik, R., San, O., Rasheed, A., and Vedula, P., "Subgrid Modelling for Two-Dimensional Turbulence Using Neural Networks," *Journal of Fluid Mechanics*, Vol. 858, No. 1, Jan. 2019, pp. 122–144.
- [21] Wang, Z., Xiao, D., Fang, F., Govindan, R., Pain, C. C., and Guo, Y., "Model Identification of Reduced Order Fluid Dynamics Systems Using Deep Learning," *International Journal for Numerical Methods in Fluids*, Vol. 86, No. 4, July 2017, pp. 255–268.
- [22] Lui, H. F. S., and Wolf, W. R., "Construction of Reduced-Order Models for Fluid Flows Using Deep Feedforward Neural Networks," *Journal of Fluid Mechanics*, Vol. 872, No. 6, June 2019, pp. 963–994.
- [23] Raissi, M., "Deep Hidden Physics Models: Deep Learning of Nonlinear Partial Differential Equations," *Journal of Machine Learning Research*, Vol. 19, No. 1, Jan. 2018, pp. 932–955.
- [24] Chaturantabut, S., and Sorensen, D. C., "Nonlinear Reduced Order Modelling via Discrete Empirical Interpolation," *SIAM Journal on Scientific Computing*, Vol. 32, No. 5, May 2010, pp. 2737–2764.
- [25] Economou, T. D., Palacios, F., Copeland, S. R., Lukaczyk, T., and Alonso, J. J., "SU2: An Open Source Suite for Multiphysics Simulation and Design," *AIAA Journal*, Vol. 54, No. 3, March 2016, pp. 828–846.
- [26] Spalart, P. R., and Allmaras, S. R., "A One Equation Turbulence Model for Turbulent Flow," *Recherche Aerospatiale*, Vol. 1, No. 5, May 1993, pp. 5–21.
- [27] Piperno, S., Farhat, C., and Larroutu, B., "Partitioned Procedures for the Transient Solution of Coupled Aeroelastic Problems Part I: Model Problem, Theory and Two-Dimensional Application," *Computer Methods in Applied Mechanics and Engineering*, Vol. 124, Nos. 1–2, June 1995, pp. 79–112.
- [28] Degand, C., and Farhat, C., "A Three-Dimensional Torsional Spring Analogy Method for Unstructured Dynamic Meshes," *Computers and Structures*, Vol. 80, No. 11, Nov. 2001, pp. 305–316.
- [29] Alonso, J. J., and Jameson, A., "Fully-Implicit Time-Marching Aeroelastic Solutions," *Proceedings of 32nd AIAA Aerospace Sciences Meeting and Exhibit*, AIAA Paper 1994-0056, Jan. 1994.
- [30] Carlberg, K., Amsallem, D., Avery, P., Zahr, M., and Farhat, C., "The GNAT Nonlinear Model Reduction Method and Its Application to Fluid Dynamics Problems," *Proceedings of 6th AIAA Theoretical Fluid Mechanics Conference*, AIAA Paper 2011-3112, June 2011.
- [31] Bengio, Y., Courville, A., and Vincent, P., "Representation Learning: A Review and New Perspectives," *IEEE Transactions on Pattern Analysis and Machine Intelligence*, Vol. 35, No. 8, Aug. 2013, pp. 1798–1828.
- [32] Sorensen, D. C., and Embree, "A DEIM Induced CUR Factorization," *SIAM Journal of Scientific Computing*, Vol. 38, No. 3, March 2016, pp. 1454–1482.
- [33] San, O., and Maulik, R., "Neural Network Closures for Nonlinear Model Order Reduction," *Advances in Computational Mathematics*, Vol. 44, No. 6, Dec. 2018, pp. 1717–1750.
- [34] Cho, K., Bahdanau, D., Bougares, F., Schwenk, H., and Bengio, Y., "Learning Phrase Representations Using RNN Encoder Decoder for Statistical Machine Translation," *Proceedings of the Conference on Empirical Methods in Natural Language Processing (EMNLP)*, Assoc. for Computational Linguistics, Doha, Qatar, Oct. 2014, pp. 1724–1734.
- [35] Shwartz, S. S., and Ben-David, S., *Understanding Machine Learning: From Theory to Algorithms*, Cambridge Univ. Press, Cambridge, England, U.K., 2014, p. 269.
- [36] Kingma, D. P., and Ba, J., "Adam: A Method for Stochastic Optimization," *Proceedings of the 3rd International Conference on Learning Representations (ICLR)*, May 2015, pp. 1–15.
- [37] Werbos, P., "Backpropagation Through Time: What It Does and How to Do It," *Proceedings of the IEEE*, Vol. 78, No. 10, Oct. 1990, pp. 1550–1560.
- [38] Lipton, Z. C., Berkowitz, J., and Elkan, J., "A Critical Review of Recurrent Neural Networks for Sequence Learning," *Proceedings of the ACM International Conference on Multimedia—MM'14*, 2014, pp. 675–678.
- [39] Hochreiter, S., and Schmidhuber, J., "Long Short-Term Memory," *Neural Computation*, Vol. 9, No. 8, Aug. 1997, pp. 1735–1780.
- [40] Kamick, P. T., and Venkatraman, K., "Shock Boundary Layer Interaction and Energetics in Transonic Flutter," *Journal of Fluid Mechanics*, Vol. 832, No. 12, Dec. 2017, pp. 212–240.
- [41] Halder, R., Damodaran, M., and Khoo, B. C., "A Signal Interpolation Approach Augmented Linear Non-Intrusive Reduced Order Model for Aeroelastic Applications," *AIAA Journal*, Vol. 58, No. 1, Jan. 2020, pp. 426–444.

K. Taira
Associate Editor